Relative dispersion of a scalar plume in a turbulent boundary layer

Q. LIAO[1]† AND E. A. COWEN[2]

[1]Department of Civil Engineering and Mechanics, University of Wisconsin–Milwaukee,
Milwaukee, WI 53211, USA

[2]DeFrees Hydraulics Laboratory, School of Civil and Environmental Engineering,
Cornell University, Ithaca, NY 14850, USA

The relative dispersion of a scalar plume is examined experimentally. A passive fluorescent tracer is continuously released from a flush-bed mounted source into the turbulent boundary layer of a laboratory-generated open channel flow. A two-dimensional particle image velocimetry–laser-induced florescence (PIV–LIF) technique is applied to measure the instantaneous horizontal velocity and concentration fields. Measured results are used to investigate the relationship between the boundary-layer turbulence and the evolution of the distance-neighbour function, namely the probability density distribution of the separation distance between two marked fluid particles within a cloud of particles. Special attention is paid to the hypothesis that a diffusion equation can describe the evolution of the distance-neighbour function. The diffusion coefficient in such an equation, termed the 'relative diffusivity', is directly calculated based on the concentration distribution. The results indicate that the relative diffusivity statistically depends on particle separation lengths instead of the overall size of the plume. Measurements at all stages of the dispersing plume collapse onto a single curve and follow a 4/3 power law in the inertial subrange. The Richardson–Obukhov constant is estimated from the presented dataset. The relationship between the one-dimensional (1D) representation of the distance-neighbour function and its three-dimensional (3D) representation is discussed. An extended model for relative diffusivity beyond the inertial subrange is proposed based on the structure of the turbulent velocity field, and it agrees well with measurements. The experimental evidence implies that, while the diffusion of the distance-neighbour function is completely determined by the underlying turbulence, the overall growth rate of the plume is affected by both the turbulent flow and its actual concentration distribution.

Key words: mixing and dispersion, turbulent boundary layers, turbulent mixing

1. Introduction

The concept of relative dispersion was first introduced by Richardson (1926), who contended that the dispersion rate of a group of marked fluid elements in a turbulent medium depends on the characteristic size of the cloud of marked elements. According to empirical analysis on atmospheric diffusion data, he concluded that for a dispersing

† Email address for correspondence: liao@uwm.edu

cloud or puff, the turbulent diffusivity is proportional to the four-thirds power of the cloud's characteristic size, i.e. the '4/3 law'. More rigorous analysis was given by Batchelor (1952) based on Kolmogorov's similarity hypothesis (Kolmogorov 1941). Since then, there have been many theoretical and experimental studies focused on relative dispersion. A thorough review was given by Monin & Yaglom (1975) and more recently by Sawford (2001).

Relative dispersion can be explained by considering the mean-square separation of two simultaneously dispersing fluid elements, hereinafter referred to as particles. Assuming high-Reynolds-number turbulence and local isotropy, if the separation distance l is within the inertial range ($\eta \ll l \ll L$, where η is the Kolmogorov length scale and L is the integral length), similarity analysis indicates that

$$\overline{l^2} - l_0^2 = g\epsilon t^3, \tag{1.1}$$

where ϵ is the dissipation rate of turbulent kinetic energy, l_0 is the initial separation distance between marked particles at $t = 0$ and g is a universal constant (Obukhov 1941), known as the Richardson–Obuhkov constant. Batchelor (1952) emphasized the importance of the initial separation l_0. He argued that (1.1) is only true for $t \gg t_0$, where $t_0 = (l_0^2/\epsilon)^{1/3}$, the time after which the Lagragian velocities of the two particles become uncorrelated. According to dimensional analysis, Batchelor pointed out that

$$\overline{l^2} - l_0^2 = \frac{11}{3}C(\epsilon l_0)^{2/3}t^2, \quad t < t_0, \tag{1.2}$$

revealing a linear (in time) growth rate regime.

Earlier experimental studies were devoted to verifying the Richardson–Obukhov scaling (1.1) through observations of tracer plumes or clouds, assuming that the size of a cloud is proportional to the mean-square particle separation. Many of these studies claimed to observe the 4/3 law (or t^3 growth of the mean-square separation distance) in the surface mixed layer of oceans or lakes (Stommel 1949; Csanady 1963; Okubo 1971), near the bed in coastal areas (Stacey *et al.* 2000), or in the atmosphere boundary layer (Gifford 1957), based on the estimated diffusivity, cloud (plume) growth rate or the decay rate of the mean centreline concentration. Based on the same theoretical grounds, Fong and Stacey's field measurement (Fong & Stacey 2003) of a bottom released dye plume in the coastal ocean shows a length scale squared law for diffusivity, where the scale of the plume falls into the two-dimensional (2D) turbulence regime.

Recently, the Lagrangian trajectories of particle pairs have been measured directly in the laboratory as well as through direct numerical simulation (DNS). By optically tracking three-dimensional (3D) trajectories of particles in grid-generated turbulence, Ott & Mann (2000) observed the Richardson–Obukhov law (1.1). It is rather surprising because the Reynolds number of the flow is low (the largest Reynolds number based on the Taylor microscale is $R_\lambda = 104$ among their datasets). By tracking particle pairs in isotropic turbulence generated by DNS ($R_\lambda = 230$) Yeung & Borgas (2004) are able to demonstrate the linear growth rate of $\sqrt{\overline{l^2} - l_0^2}$ in time for small t (and $l_0/\eta = 1/4 \sim 256$). There is no clear evidence of the Richardson–Obukhov scaling, they argue due to the small R_λ. Bourgoin *et al.* (2006) generate a strong turbulent flow ($R_\lambda = 815$) between two coaxial counter-rotating baffled disks, and track particle pairs in 3D with high-speed digital cameras. Their data show excellent agreement with Batchelor's scaling (1.2) over a broad range of time scales (more than two decades). However, the t^3 scaling does not show up even for the highest R_λ. They thus concluded

that the Richardson–Obukhov scaling requires not only a large separation between the Kolmogorov time scale (t_η) and the integral time scale (T_L) of the turbulence, but also a large separation between t_0 and T_L (T_L/t_0 must be much larger than 10). This condition would probably not be satisfied in most practical situations, thus they conclude that the t^3 scaling should not be expected in most fluid flows.

Relative dispersion has also been described through the probability density function (p.d.f.) of the separation distances of two particles. This concept, again, was first introduced by Richardson (1926) as the 'distance neighbour function' in a one-dimensional (1D) sense (i.e. the spherically averaged separation p.d.f.). Batchelor (1952) extended it to a general 3D case and explicitly considered the joint p.d.f. of two fluid particles, denoted as $p_2(\boldsymbol{x}_1, \boldsymbol{x}_2, t_1, t_2|\boldsymbol{y}_1, \boldsymbol{y}_2, s_1, s_2)$, such that $p_2\,\mathrm{d}\boldsymbol{x}_1\,\mathrm{d}\boldsymbol{x}_2$ is the probability that one fluid particle lies in a volume element $\mathrm{d}\boldsymbol{x}_1$ centred at position $\boldsymbol{x}_1$ and time t_1 and the other lies in a volume element $\mathrm{d}\boldsymbol{x}_2$ centred at position $\boldsymbol{x}_2$ and time t_2, given their initial positions are $\boldsymbol{y}_1$ and $\boldsymbol{y}_2$ at the initial times s_1 and s_2, respectively. The two-particle p.d.f. is of practical interest because the two-point concentration correlation that results from a source $S(\boldsymbol{y}, s)$ can be related to p_2 as

$$\overline{c(\boldsymbol{x}_1, t_1)c(\boldsymbol{x}_2, t_2)} = \int_{s_1 \leqslant t_1} \int_{s_2 \leqslant t_2} \int_V \int_V p_2(\boldsymbol{x}_1, \boldsymbol{x}_2, t_1, t_2|\boldsymbol{y}_1, \boldsymbol{y}_2, s_1, s_2)$$
$$\times S(\boldsymbol{y}_1, s_1)S(\boldsymbol{y}_2, s_2)\,\mathrm{d}\boldsymbol{y}_2\,\mathrm{d}\boldsymbol{y}_1\,\mathrm{d}s_2\,\mathrm{d}s_1. \quad (1.3)$$

Equation (1.3) has been the basis of a series of Lagrangian stochastic models (Durbin 1980; Thomson 1990; Borgas & Sawford 1994), through which the variance of concentration fluctuations can be modelled by simulating the velocities and trajectories of particle pairs.

If only relative dispersion is considered, also assuming the turbulence is homogeneous and letting $t_1 = t_2 = t$, $s_1 = s_2 = s$, denoting $\boldsymbol{x}_2 = \boldsymbol{x}_1 + \Delta$, $\boldsymbol{y}_2 = \boldsymbol{y}_1 + \Delta_0$, then

$$p_\Delta(\Delta, t|\Delta_0, s) = \int p_2(\boldsymbol{x}_1, \boldsymbol{x}_1 + \Delta, t|\boldsymbol{y}_1, \boldsymbol{y}_1 + \Delta_0, s)\,\mathrm{d}\boldsymbol{x}_1 \quad (1.4)$$

is the separation p.d.f. where Δ and Δ_0 are separation vectors at time t and s, respectively. It is hypothesized that the evolution of p_Δ can be described by a diffusion equation (Monin & Yaglom 1975) in the (Δ, t) space:

$$\frac{\partial p_\Delta}{\partial t} = \nabla \cdot [K_R(\Delta)\nabla p_\Delta], \quad (1.5)$$

where $K_R(\Delta)$ is a relative diffusivity. For isotropic turbulence, K_R is only a function of the magnitude of separation, i.e. $K_R = K_R(\Delta)$, where $\Delta = |\Delta|$. It should be noted that the separation p.d.f. p_Δ differs from Richardson's 'distance neighbour function' (Richardson 1926) in that it is defined as a probability distribution of two particles that results from many realizations, while the distance neighbour function (denoted as $q(\boldsymbol{l}, t)$) is the probability of the separation vector $\boldsymbol{l}$ of a pair of particles among all particle pairs in a cloud at a time t. For a 'pulse'-release cloud in an isotropic turbulent flow field at time s, its distance-neighbour function q can be related to p_Δ as

$$\overline{q(\boldsymbol{l}, t)} = \int p_\Delta(\boldsymbol{l}, t|\boldsymbol{l}_0, s)\overline{q(\boldsymbol{l}_0, s)}\,\mathrm{d}\boldsymbol{l}_0, \quad (1.6)$$

and the following diffusion equation for $\overline{q(l, t)}$ is also true given (1.5) and (1.6),

$$\frac{\partial \overline{q}}{\partial t} = \nabla \cdot [K_R(l)\nabla \overline{q}], \quad (1.7)$$

where the overbar '$\overline{\quad}$' indicates ensemble averaging over many trials. Proof of (1.6) and (1.7) can be found in Appendix A. The diffusion equation for the distance-neighbour function was first proposed by Richardson (1926), which is in the same format as (1.7), except without ensemble averaging on q. Here we argue that the ensemble averaging is necessary as the relative diffusion process is random in nature and the relative diffusivity is a statistical measure of turbulent flows. For example, for a cloud whose size is smaller than the integral length of the underlying turbulent flow, q at any given time is obtained through integration over the cloud. Although the integration is effectively an ensemble averaging over many particle pairs, statistics of turbulence (including the diffusivity) may not be converged over such a small volume that is occupied by the cloud. Therefore (1.7) is not likely to be true without ensemble averaging over many trials. With this argument, we will only consider the 'ensemble averaged' distance neighbour function and use q to replace $\overline{q}$ hereinafter.

According to Richardson (1926), $K_R \sim l^{4/3}$ if l falls in the inertial subrange, i.e. the diffusivity depends on the 'instantaneous separation' l or, more appropriately, the independent phase space variable. Batchelor (1952) argued that (1.7), if true, should be so in a statistical sense, thus $K_R \sim (\sqrt{\overline{l^2}})^{4/3}$, where $\overline{l^2(t)} = \int (l \cdot l) q(l, t) \, \mathrm{d}l$.

Earlier studies simplify the diffusion equation to a one-dimensional case (Richardson 1926; Sullivan 1971):

$$\frac{\partial q}{\partial t} = \frac{\partial}{\partial l} \left[K_R(l) \frac{\partial q}{\partial l} \right]. \tag{1.8}$$

Self-similar solutions to (1.8) exist when the initial condition is $q(l, 0) = \delta(l)$ i.e. a Dirac delta function. For $K_R \sim l^{4/3}$,

$$q(l, t) = \frac{2}{3\sqrt{\pi}} \left(\frac{105}{8\overline{l^2(t)}} \right)^{1/2} \exp\left[-\left(\frac{105}{8} \frac{l^2}{\overline{l^2(t)}} \right)^{1/3} \right], \tag{1.9}$$

whereas from Batchelor (Batchelor 1952), $K_R = \alpha(\sqrt{\overline{l^2}})^{4/3}$, the solution is a Gaussian distribution:

$$q(l, t) = \frac{1}{\sqrt{2\pi\overline{l^2}}} \exp\left[-\frac{l^2}{2\overline{l^2}} \right]. \tag{1.10}$$

Although both solutions result in a t^3 growth rate for the second moment $\overline{l^2}$, Richardson's solution (Richardson 1926) has a much sharper shape relative to a Gaussian distribution, which implies the random separation is more intermittent. If the initial condition has a particular distribution, like in most applications, there is probably no general analytical solution for (1.8).

Moreover, if l is in the inertial subrange, the '4/3 law' implies

$$K_R = k_0 \epsilon^{1/3} l^{4/3} \quad \text{or} \quad K_R = k_0 \epsilon^{1/3} (\overline{l^2})^{2/3} \tag{1.11}$$

according to Kolmogorov's similarity hypothesis, where k_0 is a non-dimensional constant. If both k_0 and the Richardson–Obuhkov constant g are universal constants, their relation can be determined from the t^3 law (defined in (1.1)) and the self-similar solution (1.9) or (1.10). Richardson's model (Richardson 1926) indicates that

$$g = \frac{280}{243} k_0^3, \tag{1.12}$$

while Batchelor's model (Batchelor 1952) shows

$$g = \frac{8}{27}k_0^3. \tag{1.13}$$

Since turbulent flows and relative dispersion are inherently 3D processes, modern analysis on the diffusion equation has adopted its 3D format but reduced it to a 1D problem mathematically, assuming isotropy (Ouellette *et al.* 2006; Salazar & Collins 2009):

$$\frac{\partial}{\partial t}q(l,t) = \frac{1}{l^2}\frac{\partial}{\partial l}\left[l^2 K_R(l,t)\frac{\partial q(l,t)}{\partial l}\right], \tag{1.14}$$

where $q(l,t)$ is the spherically averaged p.d.f. of separation, and, due to the normalization of the p.d.f.,

$$\int_V q(\boldsymbol{l},t)\,\mathrm{d}\boldsymbol{l} = \int_0^\infty 4\pi l^2 q(l,t)\,\mathrm{d}l = 1. \tag{1.15}$$

The mean-square separation is $\overline{l^2(t)} = \int_0^\infty l^2 q(l,t)4\pi l^2 \,\mathrm{d}l$.

With the 4/3 law speculated in (1.11), and the initial condition $q(l,0) = \delta(l)$ (i.e. releasing from a point source), the self-similar solution to (1.14) based on Richardson's model (Richardson 1926) is

$$q(l,t) = \frac{429}{70}\sqrt{\frac{143}{2}}\left(\frac{1}{\pi \overline{l^2(t)}}\right)^{3/2}\exp\left[-\left(\frac{1287}{8}\frac{l^2}{\overline{l^2(t)}}\right)^{1/3}\right], \tag{1.16}$$

and the solution based on Batchelor's model (Batchelor 1952) is

$$q(l,t) = \left(\frac{2\pi}{3}\overline{l^2}\right)^{-3/2}\exp\left(-\frac{3}{2}\frac{l^2}{\overline{l^2}}\right). \tag{1.17}$$

Both of the solutions result in a t^3 law for the growth of $\overline{l^2}$. However, the relation between k_0 and g is different: Richardson's model results in

$$g = \frac{1144}{81}k_0^3 \tag{1.18}$$

and from Batchelor's model,

$$g = 8k_0^3. \tag{1.19}$$

Less experimental data exist to verify the profiles of $q(l,t)$ and $p_\Delta(l,t)$. Sullivan (1971) presented the measured $q(l)$ from dye plume dispersion observations in the surface mixed layer of Lake Huron. The profile is approximately Gaussian, which agrees with Batchelor's theory. In his field experiment, the concentration of tracer dye was measured by pumping water into a fluorometer which might have destroyed the small-scale structure of the concentration field. Recently, p_Δ has been measured by tracking particle pairs in three dimensions either in laboratory flows or through DNS, and most results agreed with Richardson's model (i.e. equation (1.16)) for small initial separations (Ott & Mann 2000; Biferale *et al.* 2005; Berg *et al.* 2006; Ouellette *et al.* 2006).

There is even less experimental evidence to verify the validity of (1.5) or (1.7) and the functional form of the relative diffusivity K_R. In this paper, they are examined through measurements of 2D concentration distributions that result from a flush-bed source, continuously released tracer plume into a laboratory turbulent boundary layer. The methodology is similar to that of Sullivan (1971). For a continuously released
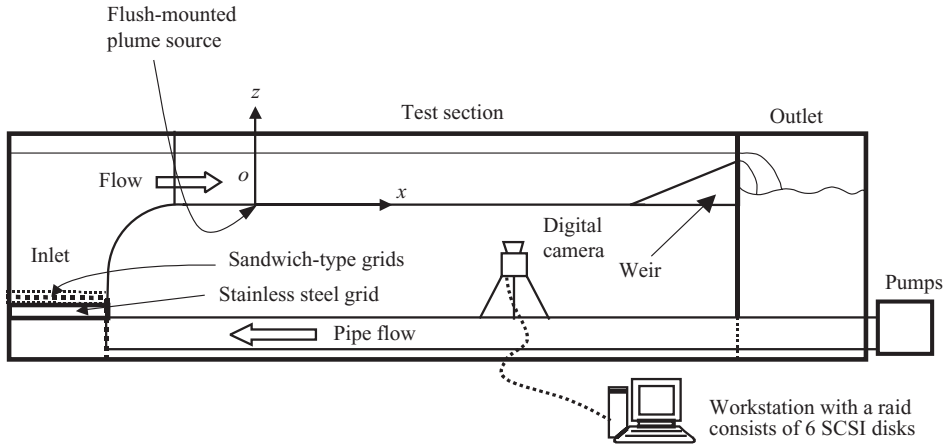
FIGURE 1. Recirculating wide open-channel flume.

scalar plume being advected by a mean flow, a 1D representation of $q(l, t)$ is related to the concentration field,

$$q(l, t) \approx q\left(l, \frac{x}{U}\right) = \frac{\int_{-\infty}^{\infty} c(x, y)c(x, y + l)\,\mathrm{d}y}{\left(\int_{-\infty}^{\infty} c(x, y)\,\mathrm{d}y\right)^2}, \qquad (1.20)$$

where x is the mean flow direction, y is the lateral direction defined based on the right-hand rule, $c(x, y)$ is the instantaneous 2D concentration field on a horizontal plane and U is the mean velocity of the advecting flow on the same horizontal plane. Using a coupled particle image velocimetry–laser-induced florescence (PIV–LIF) technique, turbulent velocities and q can be measured with high accuracy and resolution and its spatial derivatives are directly calculated. The relationship between the 1D representation of q and its 3D representation is discussed. We use the results to validate the existence of the diffusion equation for q (see (1.7)), examine the format of the relative diffusivity K_R, and estimate the Richardson–Obukhov constant g.

2. Experimental facilities and procedures
2.1. *Recirculating wide open-channel flume*
The plume dispersion experiment is conducted in a recirculating flume in the DeFrees Hydraulics Laboratory at Cornell University. As shown in figure 1, the flume consists of inlet, test and outlet sections. The test section is a 15.0 m long, 2.0 m wide and 0.64 m deep rectangular open channel with glass bottom and side walls. Water flow is driven by two axial pumps and carried into the inlet section through two 0.406 m diameter PVC pipes beneath the flume. Flow is conditioned in the inlet section by a series of grids constructed of 51 mm deep stainless steel strap with 0.10 m × 0.10 m square openings. A 25 mm thick 'horse hair' packing material layer is attached to the top of the steel grids. These materials are sandwiched between polypropylene moulded thermoplastic mesh sheets. Large vortices generated by the two pumps are broken down by the grids and a quasi-homogeneous and isotropic turbulent flow is produced. The turbulence is further conditioned by a nominally 4:1 contraction in the vertical direction before entering the test section. A 4 mm polycarbonate rod is

mounted laterally along the junction between the inlet and test sections to trip the boundary-layer turbulence. At the end of the test section, a sloping sharp crested weir is mounted to generate super-critical conditions at its crest, preventing free-surface perturbations from reflecting back into the test section.

The plume is introduced from the bottom of the flume, through a flush-bed mounted cylindrical porous stone (diameter $d = 14$ mm), which is installed at 2.25 m downstream of the leading edge of the test section and on the centreline of the channel; a passive fluorescent tracer (fluorescein solution) is pumped into the boundary layer through the porous stone. The coordinate system is defined in such a way that the centre of the source is the origin, x points downstream, in the direction of the mean flow, z is positive upwards and y is in the spanwise direction.

2.2. *Single-camera coupled particle image velocimetry–laser-induced florescence measurement technique*

The turbulent velocity and scalar concentration fields are measured simultaneously using a single-camera coupled PIV–LIF technique (Cowen, Chang & Liao 2001). The PIV–LIF measurement technique consists of capturing three images in rapid succession with a digital CCD camera. The first and third images record seed particles, illuminated by a twin-pulsed (300 mJ pulse^{-1}) 60 Hz Nd:YAG laser with illumination wavelength of $\lambda_{PIV} = 532$ nm. The two particle images are post-processed to extract the velocity fields. The second image records the fluorescent image of the scalar plume excited by the scanning beam of a 1.2 W Argon-ion continuous-wave (CW) laser with wavelength $\lambda_{LIF} = 488$ nm. This image is post-processed to yield the instantaneous scalar concentration field. Fluorescein has an absorption peak essentially coincident with λ_{LIF} and emits light over a broad range of wavelengths that begins around 490 nm, peaks at about 510 nm, and extends out beyond 600 nm (see Cowen *et al.* 2001, figure 1 for excitation and emission spectra). An optical filter is used (long-pass filter $\lambda > \lambda_c = 509$ nm) such that $\lambda_{LIF} < \lambda_c < \lambda_{PIV}$ and the majority of fluorescein emission wavelength falls into the range $\lambda > \lambda_c$. As a result, scattered light from seed particles illuminated by λ_{LIF} is rejected by the long-pass filter and is not seen in the LIF images, thus ensuring high-fidelity plume-concentration measurements. Meanwhile, since the absorption efficiency of fluorescein is low at λ_{PIV}, it only imparts a weak fluorescence signal to the PIV images, and does not adversely affect the PIV interrogation analysis. The great advantage of the technique is that two separate sets of images do not need to be referenced to each other as all information is captured on the same camera.

The two lasers and their optical systems are mounted on a vertically adjustable, rolling platform (see figure 2), allowing the generation of horizontal coplanar laser sheets at different elevations and horizontal locations within the flow.

A DALSA 1M30P CCD camera is used to acquire PIV and LIF images. It has a 12-bit grey scale pixel resolution and a spatial resolution of 1024×1024 pixels. The full-speed frame rate of the camera is 30 Hz. Captured images are streamed to a computer through a CamerLink interface and stored directly to a hard drive array in real time.

2.3. *Measurement procedures*

The plume source, a solution of fluorescein, is stored in a reservoir which is connected to the porous stone on the bottom of the flume through a plastic tube. Driven by a peristaltic pump, the tracer is pumped out from the reservoir, and runs through a two-chamber pressure fluctuation filter (Zarruk & Cowen 2008), then seeps through the porous stone into the channel with a constant rate of 120 mm^3 s^{-1}. Given the
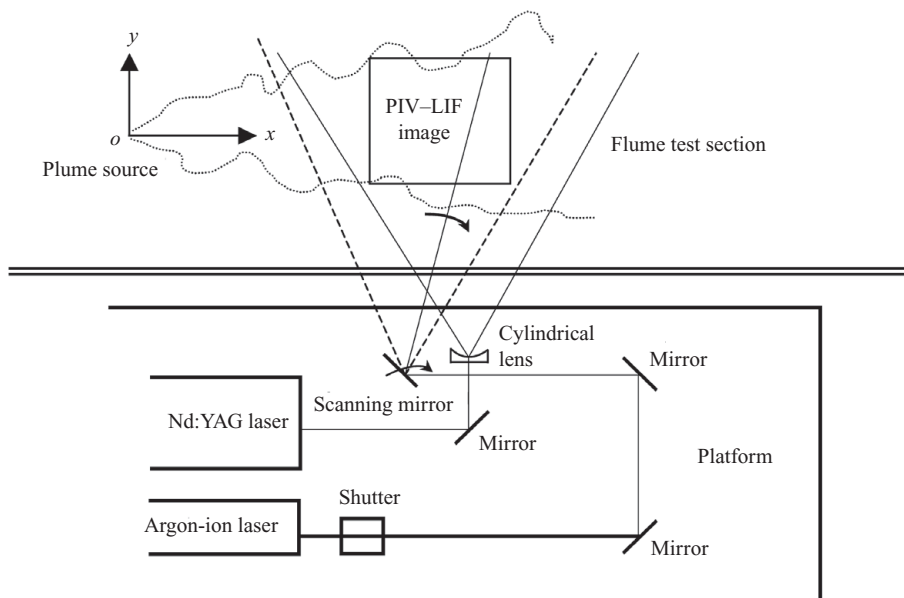
FIGURE 2. Sketch of the optical configuration of the PIV–LIF system.

diameter of the porous stone, $d = 14$ mm, the exit velocity of the plume is 0.8 mm s^{-1}. This flow is considered weak (it is about one-thirtieth of the friction velocity, the typical near-wall turbulent velocity scale) and its effect on channel boundary-layer flow structure is assumed negligible except at locations very close to the source. The mass concentration of the plume source is $C_0 = 600$ parts per million (p.p.m.). Water used to mix the fluorescein solution is taken from the flume immediately before the experiment, hence the plume is essentially neutrally buoyant. For the experiments presented in this paper, the average water depth is $H = 78.9$ mm, the depth-averaged velocity is $U_b = 0.46$ mm s^{-1}, the average friction velocity is $u_* = 22.3$ mm s^{-1}, estimated by fitting the measured vertical profiles of mean velocity with the log-law, and the momentum thickness Reynolds number is $Re_\theta = 1600$.

Velocity and concentration fields of the dispersing plume are measured at two elevations, $z = 12$ mm and $z = 24$ mm ($z^+ = 200$ and $z^+ = 400$, respectively, where $^+$ indicates wall unit scaling, i.e. normalized by the viscous length $z_v = \nu/u_*$, and ν is the kinematic viscosity of water with the measured temperature of $14°$C). The digital camera is placed underneath the tank, viewing vertically upwards. Measurements are taken at 12 sections in the streamwise direction, covering a distance $x = 0.225$–6.73 m ($16d \sim 480d$). At each measurement section, the field of view (FOV) of the images is 0.45 m $\times 0.45$ m. Hence, image resolution is 0.44 mm pixel^{-1}, i.e. about 1.8η per pixel and 1.4η per pixel for the two measurement elevations, where $\eta \equiv (\nu^3/\epsilon)^{1/4}$ is the Kolmogorov length scale of the turbulence, and the dissipation rate ϵ is estimated experimentally from the PIV results (see §3.2). The PIV images are processed following procedures described in Liao & Cowen (2005) to achieve high subpixel accuracy. Through PIV interrogations, the 2D velocity field is evaluated on a 256×256 grid, thus the resolution for velocity measurements is 4 image pixels (7.2η and 5.6η for the two elevations, respectively). The interrogation subwindow has side lengths of 16×16 pixels. Resolution for LIF measurements is considered the same as that of

x (m)	H (cm)	U_b (cm s^{-1})	u_* (cm s^{-1})	Re_θ	Re_τ	Re_R	Re_x
0.565	8.19	43.7	2.12	1600	1340	24 700	191 000
1.885	7.99	45.1	2.21	1520	1360	25 500	657 000
3.675	7.75	46.3	2.26	1580	1360	26 200	1 314 000
5.587	7.63	46.8	2.23	1690	1310	26 400	2 019 000

TABLE 1. Flow conditions at different streamwise locations.

the image itself, i.e. 0.44 mm pixel^{-1}. It should be noted that the smallest scale of scalar fluctuations is of the order of the Batchelor scale, η_B. The Schmidt number for fluorescein in water is $Sc = 1950$, thus $\eta_B = \eta/\sqrt{Sc} = 0.0226\eta$. The current image resolution is considerably larger than the smallest scalar 'eddies'. In addition, the Argon laser sheet in the measurements is about 2 mm thick ($\sim$5 pixels), hence the true LIF resolution is even coarser than the image resolution; it is estimated to be $O(\eta)$ or $O(100\eta_B)$.

For measurements at each section, image acquisition starts 2 min after the plume is initiated. 400 image triples are acquired at a rate of 2 Hz (a duration of 200 s). Since the flume is a recirculating type and the estimated recirculation time is 50 s, background contamination is noticeable at the end of each experiment. Nevertheless, the observed highest concentration of the background contamination is rather low (about 3 counts on our 12-bit sensor), thus it can be neglected. Measurements at every section and elevation are calibrated, following the steps described in Cowen *et al.* (2001), to account for effects of laser light energy fluctuation, attenuation, scanning speed of the laser beam, and the optical vignetting effect of the camera lens. The flume is drained and refilled after each measurement. It took 10 days to acquire the entire dataset. There are some measurement-to-measurement variations across the overall experiment, due to variations in the water temperature, pump speed, release rate of the plume source, etc. These variations are noticeable as will be shown in the discussion that follows; however, they are small and taken to be negligible.

In order to fully characterized the turbulent flow structures, PIV measurements are made on vertical planes along the centreline of the flume. They are taken at four sections, centred at $x = 0.565$, 1.885, 3.675 and 5.585 m. The FOV of all these vertical planes is 9.05 cm $\times$ 9.05 cm, covering the entire water depth.

3. Characteristics of the turbulent flow field

3.1. *Vertical structure of the turbulent boundary layer*

The flume utilized for this study was constructed with a fixed horizontal bed (zero bed slope) hence the flow is not uniform in the streamwise direction; the water depth H decreases and the mean flow speed accelerates with downstream distance. Table 1 lists the basic flow conditions measured by PIV at the four vertical planes along the flume centreline. $U_b \equiv (1/H) \int_0^H U \, dz$ denotes the depth-averaged mean velocity on the centreline of the flume; u_* is the friction velocity; Re_θ is the momentum thickness Reynolds number, $Re_\tau \equiv U_b H / \nu$ is the friction velocity Reynolds number, $Re_R \equiv U_b R / \nu$, where R is the hydraulic radius, and $Re_x \equiv U_b x / \nu$. A scaling analysis of the longitudinal momentum equation indicates that

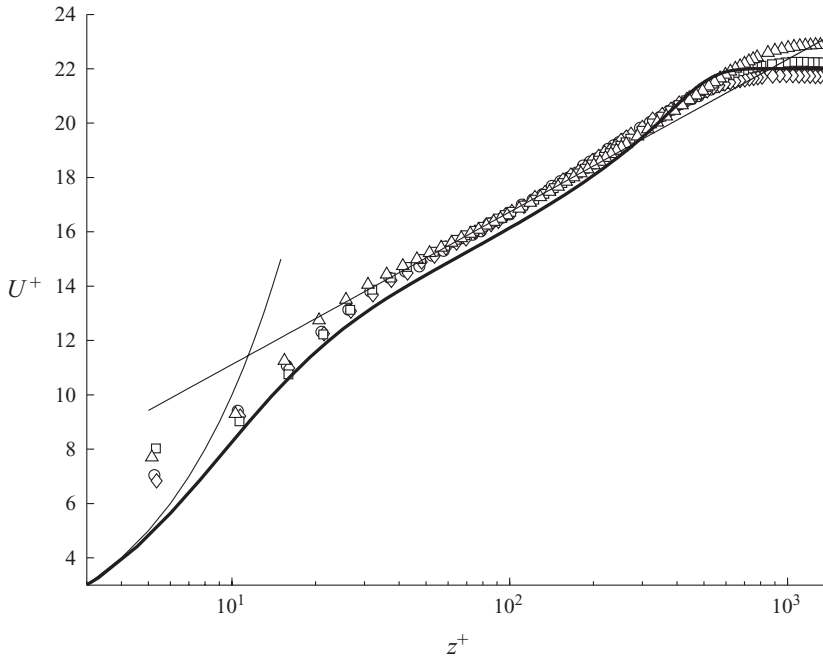$$\frac{\partial U_b^2}{\partial x} = -g \frac{\partial H}{\partial x} - \frac{u_*^2}{H}, \tag{3.1}$$

FIGURE 3. Vertical profiles of mean streamwise velocity measured at four locations. ○, $x = 0.56$ m; ◇, $x = 1.88$ m; □, $x = 3.67$ m; △, $x = 5.58$ m; thin solid line, log-law profile and viscous sublayer linear profile; bold solid line, DNS result.

where the streamwise acceleration can be approximated as $\partial U_b^2/\partial x \sim 0.0056$ (cm s^{-2}), the estimated streamwise hydrostatic pressure gradient is $-g(\partial H/\partial x) \sim 0.58$ (cm s^{-2}) and the averaged bottom friction $-u_*^2/H \sim -0.61$ (cm s^{-2}). Thus the streamwise acceleration can be neglected.

Vertical profiles of wall-scaled mean streamwise velocities $U^+ \equiv U/u_*$ at four downstream locations are shown in figure 3. The friction velocities u_* are estimated by least squares fitting the measured profiles with the log-law:

$$\frac{U(z)}{u_*} = \frac{1}{\kappa} \log \frac{z u_*}{\nu} + C, \qquad (3.2)$$

where $\kappa = 0.41$, is von Kármán's constant, and C is a constant taken to be 5.5. The DNS results of the flat-plate turbulent boundary-layer simulation of Spalart (1988) ($Re_\theta = 1410$) are also shown in this figure for comparison. The PIV measurements agree very well with the log-law for $30 < z^+ < 200$ at all measurement locations. The DNS profile in the log-law region is slightly lower than our measurement, and its best fit C is 5.0 instead of 5.5. This observation is consistent with Cowen & Monismith (1997), who argued that it is because the flume bottom is not perfectly smooth, compared to that in the DNS.

Figure 4 shows the profiles of the root-mean-square (r.m.s.) velocity fluctuations, δ_u and δ_w, and the Reynolds stress $-\overline{u'w'}$ in the wall region for $z^+ < 400$. The comparison with DNS results, while good near the wall, deviates away from the wall, particularly for the streamwise velocity fluctuations. This is expected as the DNS is for an idealized boundary layer with no turbulence sources other than the wall. The higher turbulent fluctuations away from the wall are the result of the advection of decaying inlet-grid
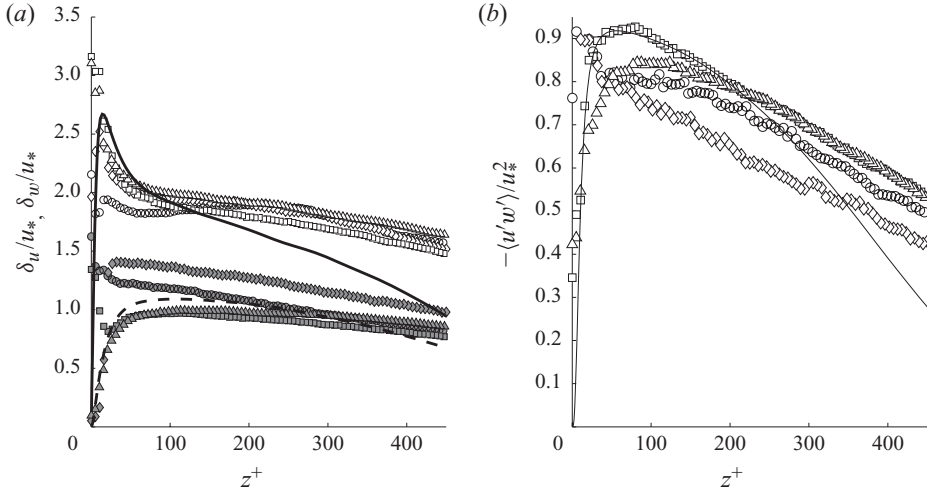
FIGURE 4. (*a*) Vertical profiles of the r.m.s. velocity fluctuations measured at four locations. (*b*) Vertical profiles of the Reynolds stress. For both (*a*) and (*b*), symbols represent measured results: $\circ$, $x = 0.56$ m; $\diamond$, $x = 1.88$ m; $\square$, $x = 3.67$ m; $\triangle$, $x = 5.58$ m; bold solid line, δ_u from DNS; bold dashed line, δ_w from DNS; thin solid line, $-\overline{u'w'}$ from DNS.

generated turbulence. For the region between $150 < z^+ < 450$, turbulent fluctuations are relatively uniform (with variations less than 10 %). Measurements of horizontal dispersion are made at $z^+ = 200$ and 400, in an effort to avoid the effects of the inhomogeneous turbulence in the boundary layer.

3.2. *Turbulence characteristics*

The most important parameter for turbulent relative dispersion is the dissipation rate of turbulent kinetic energy, ϵ, which attests to the 'small-scale' universality of turbulent flows under a statistically equilibrium state, despite various forms of 'large-scale' forcings. The dissipation rate of turbulent kinetic energy is defined as

$$\epsilon \equiv \frac{1}{2}\nu \overline{\left(\frac{\partial u_i}{\partial x_j} + \frac{\partial u_j}{\partial x_i}\right)\left(\frac{\partial u_i}{\partial x_j} + \frac{\partial u_j}{\partial x_i}\right)} = \nu \overline{\frac{\partial u_i}{\partial x_j}\left(\frac{\partial u_i}{\partial x_j} + \frac{\partial u_j}{\partial x_i}\right)}. \tag{3.3}$$

It is a summation of 12 independent terms while only six of them are available from a 2D PIV measurement. If the turbulence is locally isotropic, as hypothesized by Kolmogorov (1941) for sufficiently high Re turbulence, (3.3) becomes $\epsilon = 15\nu\overline{(\partial u/\partial x)^2}$. Boundary layer turbulence in laboratory flows is not expected to be locally isotropic at small Re. Based on experimental studies, Saddoughi & Veeravalli (1994) established a criterion for local isotropy in turbulent shear flows, $S_c^* \equiv S(\nu/\epsilon)^{1/2} < 0.01$, where S is the mean strain rate ($S = \partial U/\partial z$ in a 2D boundary-layer flow). In the present case, it is estimated that $S_c^* = 0.20$ and 0.13, for $z^+ = 200$ and $z^+ = 400$, respectively, hence the turbulence is locally anisotropic. George & Hussein (1991) propose that turbulence is locally axisymmetric for a turbulent boundary layer, i.e. statistics of velocity derivatives are invariant with respect to rotation of a preferred axis (along the mean streamwise direction in the present case). As a result, the dissipation rate becomes

$$\epsilon_A = \nu \overline{\left[-\left(\frac{\partial u}{\partial x}\right)^2 + 8\left(\frac{\partial v}{\partial y}\right)^2 + 2\left(\frac{\partial u}{\partial y}\right)^2 + 2\left(\frac{\partial v}{\partial x}\right)^2\right]}, \tag{3.4}$$
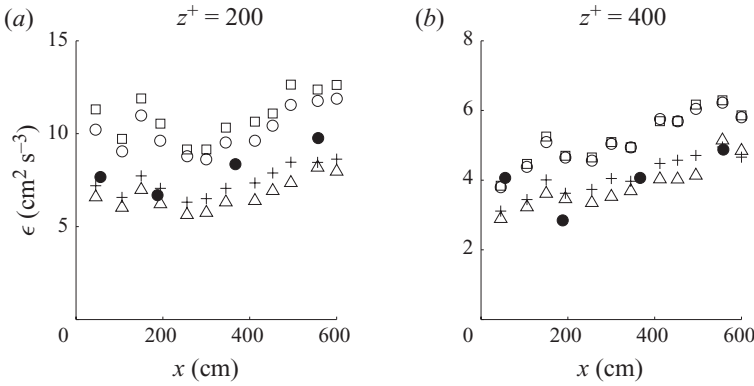
FIGURE 5. Estimated turbulent kinetic energy dissipation rate using different methods.
○, ϵ_{ux}; □, ϵ_{vy}; +, ϵ_{vx}; △, ϵ_A; ●, ϵ_p.

where the subscript 'A' denotes that ϵ is obtained by assuming local axisymmetry. In the present study, local axisymmetry is considered as a reasonable approximation, hence the dissipation rate is determined from 2D PIV measurements on horizontal planes using (3.4). Finite differencing is applied to estimate the spatial gradients of velocities. Cowen & Monismith (1997) estimated that 99 % of dissipation would be included with finite differencing if the PIV grid size is smaller than 5.5η. Thus the PIV grid resolution (1.8 mm) in some cases is slightly coarser than that required for using direct differentiation to estimate ϵ (in the worst case, the PIV resolution is 7.3η), thus slightly underestimating ϵ_A. For the measurement section, $x = 3.22 \sim 3.67$ m, $\epsilon_A = 9.8\nu\overline{(\partial u/\partial x)^2}$ for $z^+ = 200$ and $\epsilon_A = 10.4\nu\overline{(\partial u/\partial x)^2}$ for $z^+ = 400$ compared to $\epsilon = 15\nu\overline{(\partial u/\partial x)^2}$ for locally isotropic turbulence. For each of the 12 streamwise sections, one value of ϵ_A is calculated by averaging over all the PIV interrogation grid points on horizontal planes and over time. The result is considered as an estimation of the dissipation rate at the centre point of the current FOV. Figure 5 shows the streamwise distribution of estimated ϵ_A (triangles).

In the log-law region, the dissipation rate is approximately in balance with the production rate. Thus the dissipation rate can be estimated by this assumption, denoted as ϵ_P, and

$$\epsilon_P = \mathscr{P} \equiv -\overline{u'w'}\frac{\partial U}{\partial z}. \tag{3.5}$$

For the four streamwise locations where vertical 2D PIV measurements are available, ϵ_P is obtained from the vertical profiles of $U(z)$ and the Reynolds stress $\overline{u'w'}(z)$. As shown in figure 5, ϵ_P agrees with ϵ_A well.

The 1D velocity spectra for the two velocity components $u(x, y)$ and $v(x, y)$ measured on horizontal planes are also calculated for each measurement section. It is assumed that velocity fluctuations are statistically homogeneous on horizontal planes, thus spectra are calculated directly without invoking Taylor's frozen turbulence assumption. As an example, spectra of u and v along the streamwise and spanwise directions, i.e. $E_{ux}(\kappa_x)$, $E_{vx}(\kappa_x)$, $E_{uy}(\kappa_y)$ and $E_{vy}(\kappa_y)$, measured at section $x = 3.22 \sim 3.67$ m and elevation $z^+ = 400$ are shown in figure 6, where κ_x and κ_y are wavenumbers in the streamwise and spanwise directions, respectively. Three of the four 1D spectra show a $-5/3$ slope which spans slightly less than one decade, the exception being E_{uy}. A local peak at $\kappa = 2\pi/l_s$ appears for E_{uy}, where $l_s \approx 0.25$ m. This
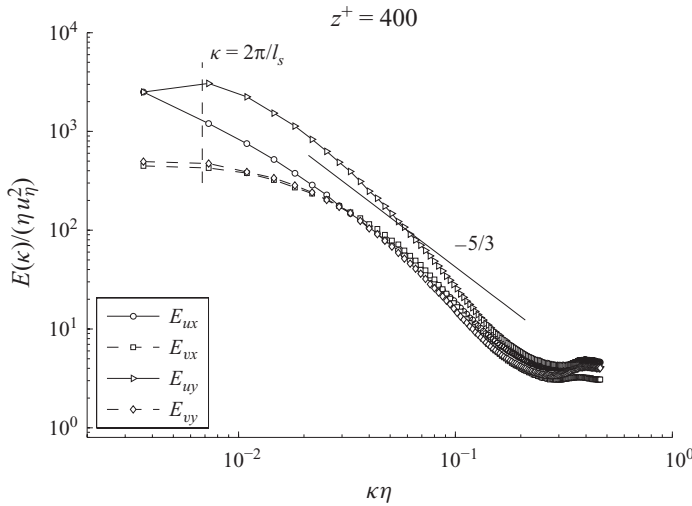
FIGURE 6. Typical 1D velocity spectra, measured at section $x = 3.22 \sim 3.67$ m and elevation $z^+ = 400$. Spectra are normalized by the Kolmogrov's length scale and velocity scale, η and u_η.

is evidence of the cellular secondary flow structure which is common in open-channel flows (Vanoi 1946; Karcz 1966). Measured $U(x, y)$ also exhibit spanwise variations with an almost sinusoidal pattern and each flow cell pair is separated by about 0.25 m. There is, however, no obvious evidence that the secondary flow structures contaminate the other three 1D spectra.

The 1D velocity spectra also indicate that the turbulence is not locally isotropic even thought the $-5/3$ slope is present. Over the inertial subrange scales, $E_{vx}/E_{vy} = 1.14$ at $z^+ = 200$ and 1.21 at $z^+ = 400$, while it should be 4/3 if locally isotropic (Pope 2000). Dissipation rate can also be estimated by fitting the measured E_{ux} and E_{vy} (the $-5/3$ region) with the universal longitudinal velocity spectrum $E_{LL}(\kappa) = (18/55)C\epsilon^{2/3}\kappa^{-5/3}$ and by fitting E_{vx} with the transverse velocity spectra $E_{NN}(\kappa) = (24/55)C\epsilon^{2/3}\kappa^{-5/3}$. The obtained dissipation rates are denoted as ϵ_{ux}, ϵ_{vy} and ϵ_{vx}, respectively, and they are also shown in figure 5 for comparison. Because of anisotropy, they are definitely biased estimates of the true ϵ. The two longitudinal estimates ϵ_{ux} and ϵ_{vy} agree well and are substantially higher than ϵ_A, while the transverse estimation ϵ_{vx} is only slightly higher than ϵ_A. All spectral estimates maintain a constant ratio with ϵ_A at all of the 12 measurement sections.

In estimating the dissipation rate in a coastal ocean boundary layer using a submersible PIV system, Doron *et al.* (2001) proposed a variety of methods including the first two methods introduced here. Their results also demonstrate that ϵ deduced from the spectral methods are higher than those from 'direct' methods. In the following analysis, we will use ϵ_A as the estimated dissipation rate.

The turbulent kinetic energy k is obtained at locations where both horizontal and vertical PIV measurement results are available. Along with the estimated dissipation rate, the length scales of the turbulence, including the characteristic size of the large eddy L, the Kolmogorov length scale η and the Taylor microscale λ are readily obtained by

$$L = \frac{k^{3/2}}{\epsilon}, \quad \eta = \left(\frac{\nu^3}{\epsilon}\right)^{1/4}, \quad \lambda = \sqrt{\frac{10\nu k}{\epsilon}}. \tag{3.6}$$

	$z^+ = 200$			$z^+ = 400$		
x (m)	0.45	1.5	5.0	0.45	1.5	5.0
ϵ (mm^2 s^{-1})	627	665	700	289	362	413
η (mm)	0.24	0.24	0.24	0.30	0.28	0.27
L (mm)	116	110	114	140	147	112
λ (mm)	6.0	5.8	5.9	7.3	7.1	6.9
R_λ	157	153	158	156	168	168

TABLE 2. Velocity and length scales of the turbulence at the two measurement elevations.

Table 2 lists the measured length scales of the turbulence at three streamwise locations, along with the Reynolds number based on Taylor's microscale, defined as $R_\lambda = \sqrt{k}\lambda/\nu$. Most statistical values do not vary appreciably along the flow except for ϵ at $z^+ = 400$, which increases moderately with downstream distance due to the growing boundary layer. Thus the turbulent flow field can be considered as nearly homogenous in both the x and y directions in the test range of $x = 0 \sim 6$ m.

4. Horizontal relative dispersion

4.1. *Two-dimensional concentration field*

The most salient feature of a dispersing plume released from a small source in atmospheric and oceanic flows is its 'meandering' motion, which occurs due to the fact that the lateral size of plume is small compared to the size of large eddies in typical environmental flows. Eddies smaller than the size of the plume are most effective at expanding and stirring the plume, while large eddies just move the plume as a whole. Since relative dispersion is concerned only with the growth of a cloud, we have removed the meandering effects of the plume by translating the reference frame to the 'centre of mass' (COM) of the instantaneous plume, i.e. the COM reference frame $x'o'y'$ is attached to the first moment (centroid) of the instantaneous lateral concentration distribution, such that

$$x' = x, \tag{4.1}$$
$$y' = y - y_c, \tag{4.2}$$

where y_c is the COM,

$$y_c \equiv \frac{1}{A} \int_{-\infty}^{\infty} yc(y)\,\mathrm{d}y, \tag{4.3}$$

$$A \equiv \int_{-\infty}^{\infty} c(y)\,\mathrm{d}y, \tag{4.4}$$

where $c(y)$ is the instantaneous lateral concentration distribution. At the same time, the instantaneous lateral width of the plume can be defined as the second central moment of the lateral concentration distribution, i.e.

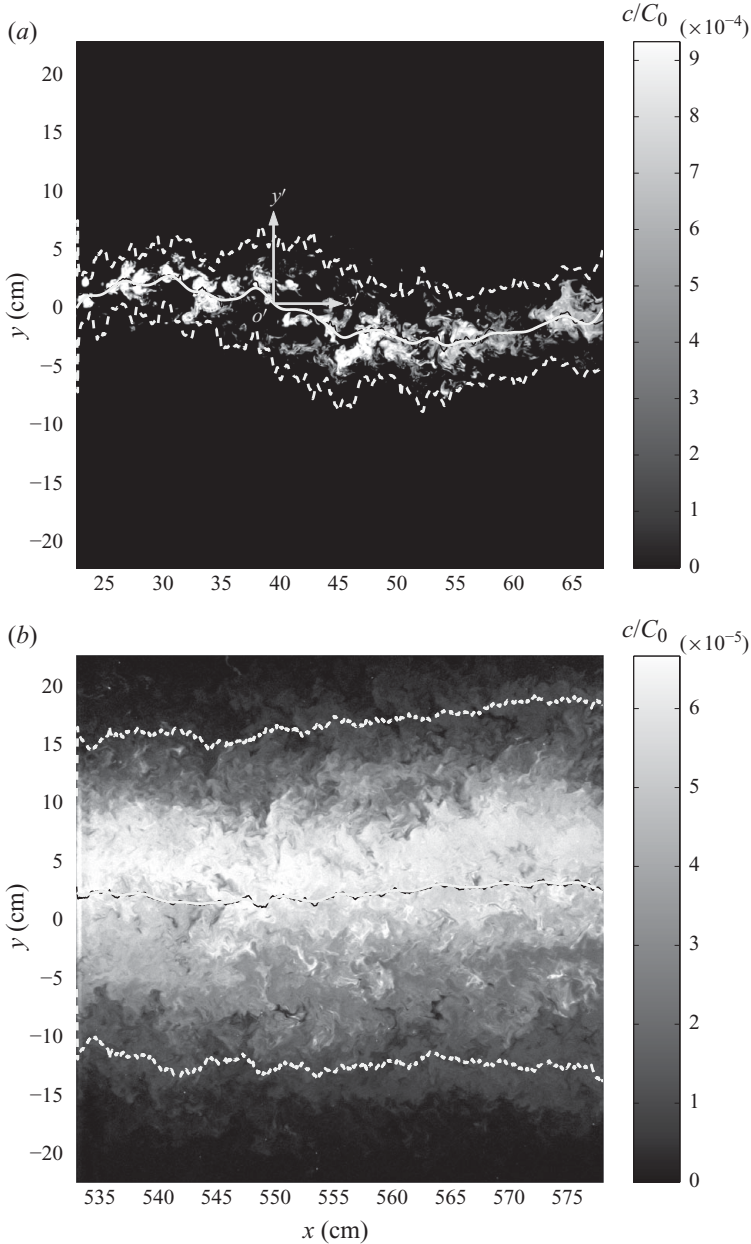$$\sigma_I^2 \equiv \frac{1}{A} \int_{-\infty}^{\infty} (y - y_c)^2 c(y)\,\mathrm{d}y. \tag{4.5}$$

FIGURE 7. Instantaneous concentration distribution of the plume in the near and far fields. The instantaneous centreline (bold white line) is smoothed by applying a Gaussian filter (with filter half-width equal to the instantaneous plume width) to the line directly calculated (black thin line) by (4.3). The dashed white lines are the e^{-2} boundaries of the plume, $y_c \pm 2\sigma_I$.

Examples of the reference frame translation are shown in figure 7, for typical near- and far-field cases. It is evident that meandering in the near field is strong as the variation of the centroid is relatively large; as the plume grows in width and the
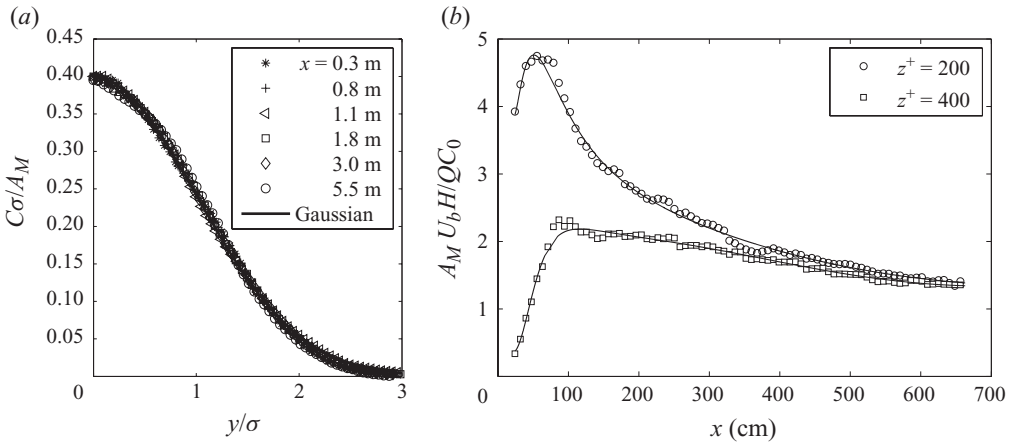
(a)

(b)

FIGURE 8. (*a*) Lateral profiles of the ensemble mean concentration in the 'COM' reference frame. (*b*) Longitudinal evolution of the normalized lateral integrated mass.

concentration field becomes smoother in the far field, the centreline appears to be 'straightened'.

The lateral mean concentration distribution in the 'COM' reference frame is obtained by ensemble averaging 400 LIF images with their instantaneous centrelines, y_c, aligned, denoted as $C \equiv \overline{c(y')}$. A Gaussian distribution $\mathscr{G}(y') = (A_M / \sqrt{2\pi}\sigma) \exp(-y'^2/2\sigma)$ is used to fit $C(y')$ at every streamwise location in a least-square sense. Fitting parameters $A_M(x)$ and σ are considered as the total mass (per unit streamwise length and depth) and the mean lateral size, respectively. Normalized mean concentration profiles $\sigma C(y')/A_M$ at six streamwise locations, $x = 0.3, 0.8, 1.1, 1.8, 3.0$ and 5.5 m, are shown in figure 8(*a*). They collapse tightly on a standard normal distribution. The streamwise evolution of the lateral integral of the concentration distributions (A_M) at the two measurement heights is shown in figure 8(*b*). They are normalized by the source flux per unit water depth, therefore normalized values approaching 1.0 indicate the dye plume is becoming vertically well mixed over the water depth. As shown in figure 8, the plume is not completely vertically well mixed even at the furthest measurement location ($x = 6.73$ m). Net upward flux is present at all measurement stations. However, the net flux is much weaker at a distance of about 3 m or further, as the gradient of $A_M(x)$ becomes small.

According to the measurements, $\overline{\sigma_I^2(x)}$ matches σ^2 very well (see figure 9). However, the latter appears smoother since background noise has been minimized by averaging. We will use σ^2 as a surrogate for $\overline{\sigma_I^2(x)}$ in the rest of this analysis, and σ is interpreted as the characteristic 'width' of the dispersing plume, which can also be considered to be half of the mean-square separation of marked fluid particles, as will be demonstrated below (see (4.8)).

The apparent diffusivity is defined as the growth rate of σ^2, i.e. $K_A \equiv (d\sigma^2/dt)/2$. Fourth-order polynomial curve fits have been applied to the measured $\sigma^2(x)$. The fitted polynomial functions are used to calculate $d\sigma^2/dx$ and the streamwise evolution of the apparent diffusivity K_A, which are shown in figure 18 in §4.5 as the solid and dashed lines. It is clear that K_A increases with distance from the plume source,
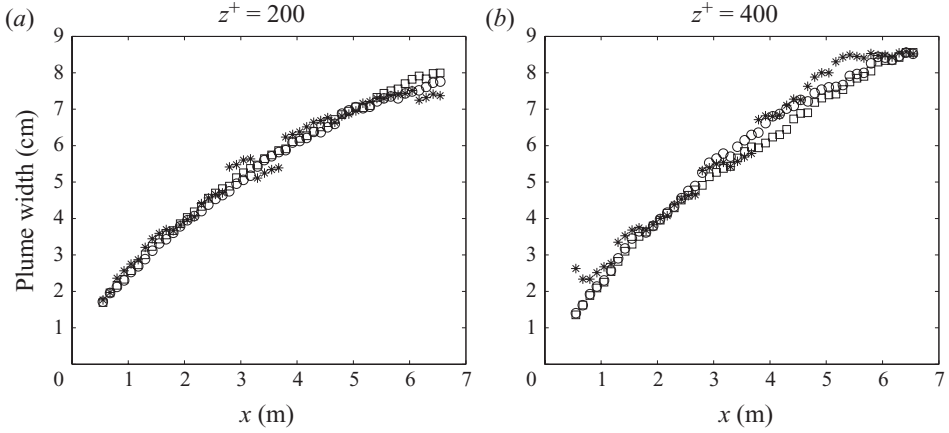
FIGURE 9. Change of the characteristic plume 'width' with streamwise location at both measurement elevations. Plume width is estimated with three different methods: $\circ$, σ, width from the mean concentration distribution in the 'COM' reference frame; $*$, $\sqrt{\overline{\sigma_I}}$, mean of instantaneous plume width; $\square$, $\sigma_Q/\sqrt{2}$, standard deviation of the 1D distance-neighbour function $Q(l, x)$.

suggesting that it depends on the size of plume, σ. It then asymptotes to a constant as the plume size reaches the integral length of the underlying turbulence. In the presented experiments, the inertial subrange of the turbulence is quite narrow (see figure 6) and the upper limit of the inertial 'eddy' size is about $6 \sim 7$ cm, which is not much larger than the lateral size of the plume even at the near source locations (e.g. see figure 7). As a result, measured K_A does not scale with $\sigma^{4/3}$ in the scale-dependent region. Nonetheless, the 4/3 law is still evident at inner scales (inertial subrange) as is shown in the following section.

4.2. Relative dispersion

Batchelor (1952) pointed out that Richardson (1926) was not able to distinguish between two different definitions of the distance-neighbour function. First, the distance-neighbour function can be interpreted as the fraction of a large number of trials for which two particles are separated by a distance l at a given time t given the same initial separation. Second, it can also be interpreted as the fraction of the total number of particle pairs that are separated by l in an instantaneous spatial distribution of a group of particles. The two definitions can be related by (1.6). It is by the second definition that we can relate the distance-neighbour function to the instantaneous concentration distribution of a scalar plume (see Appendix A). In this paper, the 1D distance neighbour function (q_y) can be obtained by calculating the self-correlation of the instantaneous concentration in the spanwise direction

$$q_y(l) = \frac{\int c(y)c(y + l)\,\mathrm{d}y}{\left(\int c(y)\,\mathrm{d}y\right)^2}. \tag{4.6}$$

According to (4.5), the second moment of $q_y(l)$, or the mean-square separation length in the spanwise direction, is proportional to the instantaneous plume size squared

$$\int_{-\infty}^{\infty} l^2 q_y(l)\,\mathrm{d}l = \int_{-\infty}^{\infty} l^2 \frac{\int c(y)c(y+l)\,\mathrm{d}y}{\left(\int c(y)\,\mathrm{d}y\right)^2}\,\mathrm{d}l$$

$$= \int_{-\infty}^{\infty}\int_{-\infty}^{\infty} (y_1 - y_2)^2 \frac{c(y_1)c(y_2)}{\left(\int c(y)\,\mathrm{d}y\right)^2}\,\mathrm{d}y_1\,\mathrm{d}y_2$$

$$= 2\int_{-\infty}^{\infty} (y - y_c)^2 \frac{c(y)}{\int c(y)\,\mathrm{d}y}\,\mathrm{d}y = 2\sigma_I^2. \tag{4.7}$$

Here, we introduce a third definition for the distance-neighbour function, which is the 'ensemble average' of $q_y(l)$ over many trials of released clouds, i.e. $Q(l) \equiv \overline{q_y(l)}$, and according to (4.7), the mean-square separation of particle pairs within the plume, denoted as σ_Q, is

$$\sigma_Q \equiv \int_{-\infty}^{\infty} l^2 Q\,\mathrm{d}l = 2\overline{\sigma_I^2} = 2\sigma^2. \tag{4.8}$$

This relation is demonstrated in figure 9 where it shows $\sigma_Q/\sqrt{2}$ matches well with both σ and $\sqrt{\overline{\sigma_I^2}}$. As has been discussed in the introduction, the ensemble averaging over the distance-neighbour function is necessary; otherwise the diffusion equation for $q(l,t)$ may not be true, since the relative diffusivity K_R is a statistic of the turbulent flow field, which requires ensemble averaging.

It should be noted that the situation described by (4.6) is not the distance-neighbour function of a single release of puff or cloud, but a continuous release of puffs. We are measuring concentration at a downstream location x from a continuous source as an approximation of following a single release of puff in time through the relation $t = x/U$. Results obtained with this approximation may affect the validity of the relation between the particle pair separation p.d.f. and the distance-neighbour function, i.e. equation (1.6).

If the evolution of the 1D distance neighbour function can be approximated as a 1D process, the evolution of Q can be described by

$$\frac{\partial Q}{\partial t} = \frac{\partial}{\partial l}\left(K_R \frac{\partial Q}{\partial l}\right), \tag{4.9}$$

following (1.8). We will examine if the four-thirds law applies to K_R and whether $K_R \sim l^{4/3}$ or $K_R \sim (\sqrt{\overline{l^2}})^{4/3} = \sigma^{4/3}$.

Since turbulence and relative dispersion are intrinsically 3D processes, it is questionable whether the 1D simplification would be appropriate. With the assumption of isotropy, the measured $Q(l,t)$ can be associated with the 3D distance-neighbour function $q(l,t)$. There are two possible interpretations, as shown in Appendix B. First, $Q(l,t)$ could be the marginal p.d.f. of the joint p.d.f. $q(l,t)$. Following this assumption, the estimated 3D form of q is denoted as q_M:

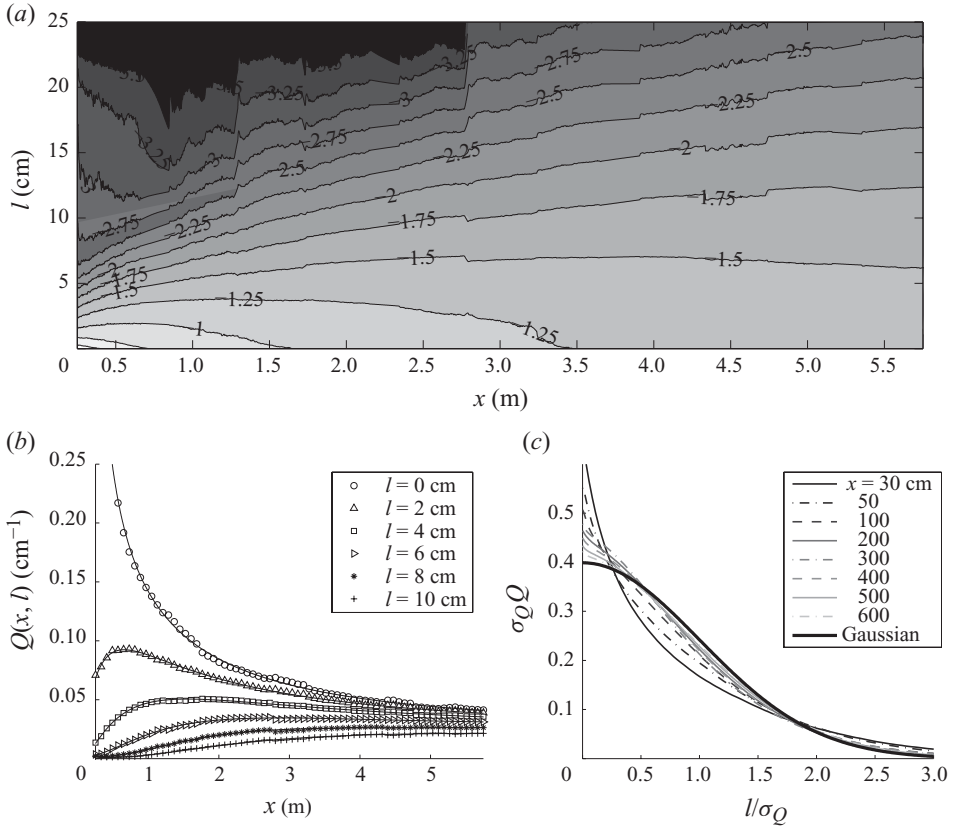$$q_M(l,t) = -\frac{1}{2\pi l}\frac{\partial Q(l,t)}{\partial l}, \tag{4.10}$$

FIGURE 10. Measured distance neighbour function $Q(x, l)$. (*a*) Map of log Q, where the unit of Q is cm^{-1}; (*b*) streamwise evolution of Q; (*c*) lateral profiles of $Q(l)$ at different downstream distances, where the black solid line represents a standard normal distribution.

and the associated relative diffusivity is denoted as K_M. Alternatively, $Q(l, t)$ can be considered to be the conditional p.d.f. of $q(l, t)$ when the separation vector is chosen to align with the *y*-axis. The estimated q following this assumption is then denoted as q_C, and

$$q_C(l, t) = \frac{Q(l, t)}{8\pi\sigma^2}, \tag{4.11}$$

with the associated relative diffusivity denoted as K_C. The two estimations of the 3D distance-neighbour function are assumed to follow the diffusion equation (1.14), and their diffusivities will be examined and compared with that in the 1D model (4.9).

Following (4.6), the 1D distance-neighbour function $Q(l)$ can be easily obtained from the measured concentration field. Figure 10(*a*) shows the map of log Q on the horizontal plane $z^+ = 200$. The measurements from the 12 sections have been patched together, and the results are very smooth in the crossflow direction, allowing direct calculation of spatial derivatives using finite differencing. The streamwise evolution of Q is shown in figure 10(*b*). Small discontinuities can be observed at junctions between two measurement sections. A fourth-order polynomial function has been fitted to log Q versus log x, shown as solid lines in the figure. The fitted polynomial functions are used to estimate $\partial Q/\partial x$, which can be converted to the time rate of change of Q as $\partial Q/\partial t = U(\partial Q/\partial x)$ where U is the local mean streamwise velocity measured by PIV.

Lateral profiles of $Q(l)$ at different downstream locations are shown in figure 10(c), scaled by the standard deviation of the separation p.d.f. (distance-neighbour function) σ_Q. They are, however, not self-similar. The shape of $Q(l)$ near the source resembles Richardson's solution (sharp gradient for small l), it then relaxes towards a Gaussian profile as x increases, rather slowly. Even at fairly far downstream distances, the shape of $Q(l)$ is still sharp compared to a Gaussian distribution. It should be noted that even if Richardson's theory were correct, we cannot expect $Q(l) \sim \exp(-l^{2/3})$ since the initial distribution has a finite size.

The estimated 3D form of the distance-neighbour functions, $q_C(l)$ and $q_M(l)$, is calculated based on (4.11) and (4.10), respectively, and their spatial derivatives are calculate using the same technique as for $Q(l)$.

The excellent resolution and coverage of the present LIF measurements allow the relative diffusivity K_R to be calculated directly. From the diffusion equation (4.9), we have

$$K_R(l, x) = \frac{U \int_0^l \dfrac{\partial Q(l', x)}{\partial x} \, \mathrm{d}l'}{\dfrac{\partial Q(l, x)}{\partial l}}, \tag{4.12}$$

where $\partial Q/\partial x$ is obtained as the derivative of the fitted lines as shown in figure 10(b), and $\partial Q/\partial l$ is obtained by direct numerical differentiation (e.g. finite difference) of the lateral profiles. For the two estimated 3D models, their relative diffusivities are also calculated directly according to (1.14), i.e.

$$K_C(l, x) = \frac{U \int_0^l l'^2 \dfrac{\partial q_C(l', x)}{\partial x} \, \mathrm{d}l'}{l^2 \dfrac{\partial q_C(l, x)}{\partial l}}, \tag{4.13}$$

$$K_M(l, x) = \frac{U \int_0^l l'^2 \dfrac{\partial q_M(l', x)}{\partial x} \, \mathrm{d}l'}{l^2 \dfrac{\partial q_M(l, x)}{\partial l}}. \tag{4.14}$$

The three calculated diffusivities are presented in figure 11, where they have been non-dimensionalized by the external turbulence scales δ_v and L. For K_R and K_C, measurements at all locations collapse well in the range $0.1 < l/L < 6$. It is clear that for $0.1 < l/L < 1$, both K_R and K_C unambiguously shows an $l^{4/3}$-dependence. This is direct evidence verifying Richardson's theory while contradicting Batchelor's argument about K_R. The 3D relative diffusivity based on the marginal p.d.f. assumption, K_M, does not show an $l^{4/3}$ regime. It does appear to follow a power function as $K_M \sim l^2$ in the inertial subrange. However, the observed l^2 law does not seem to scale with δ_v and L (nor does it scale with ϵ) since data measured at different streamwise locations do not collapse. This suggests that either the assumption that q is the marginal p.d.f. of Q is not well posed, or more parameters are required to explain the observed l^2 scaling.

4.3. *Richardson–Obukhov constant, g*

Measured $K_R(x, l)$ is plotted against $\epsilon^{1/3} l^{4/3}$ for $l < L$ in figure 12. Linear regressions are applied to determine the scaling constant k_0 in (1.11) with the intercept forced to be 0. Similarly, the scaling constant k_0 in the general 3D model can be determined from the measured K_C, following the assumption that $Q(l)$ is the conditional p.d.f. of
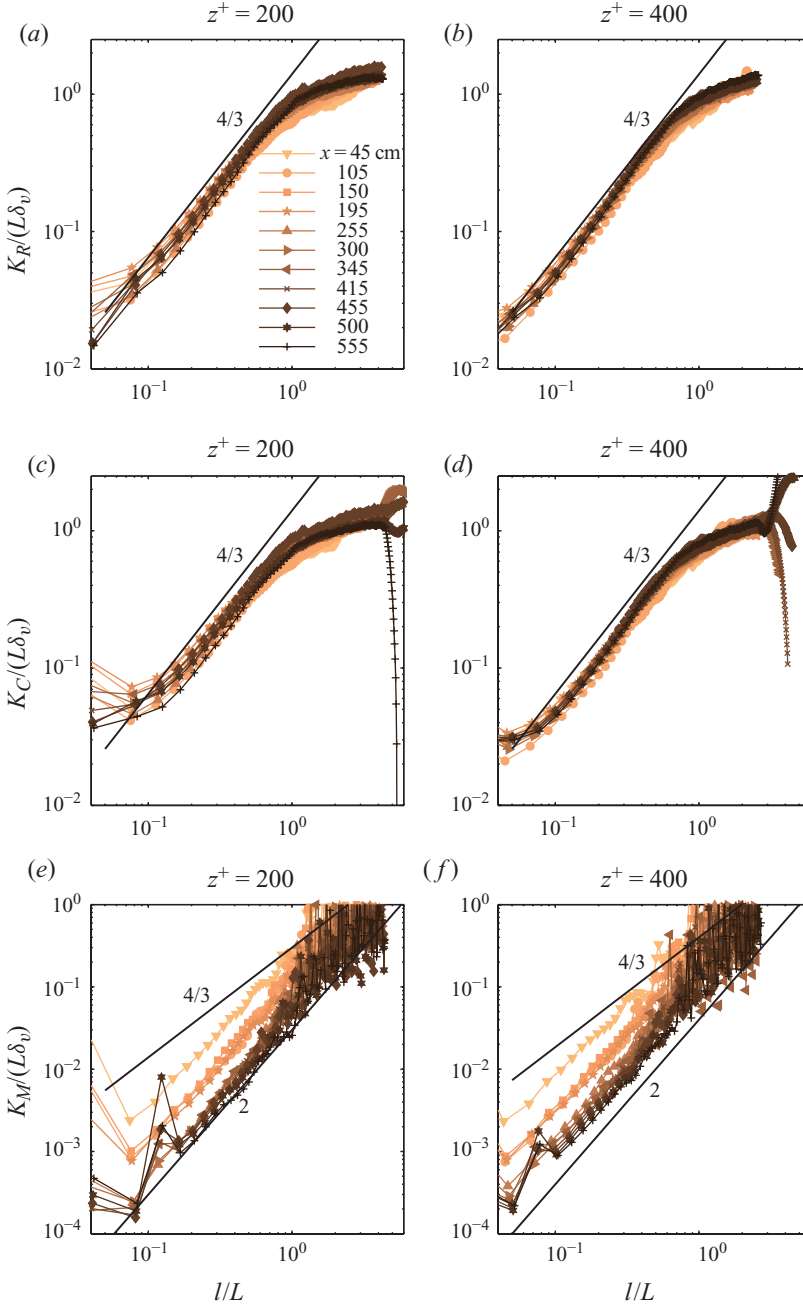
FIGURE 11. Relative diffusivities K_R, K_C and K_M as a function of separation l, measured at two elevations and at $x = 45, 105, 150, 195, 255, 300, 345, 415, 455, 500, 555$ cm, respectively.

the 3D form of $q(l)$. The distributions of k_0 along the streamwise direction from both 1D and 3D diffusion equations are presented in figure 13. Overall, k_0 estimated from both models is fairly uniform over the entire measurement range in the x direction. Again, section to section variations are noticeable.
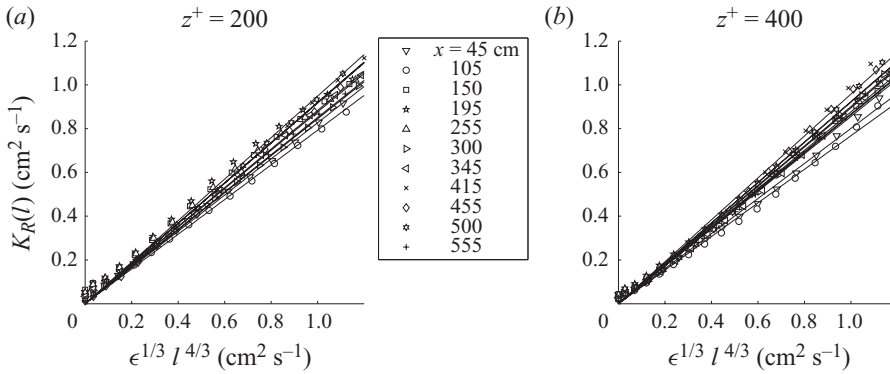
FIGURE 12. Linear relationship between the relative diffusivities K_R and the separation $l^{4/3}$. Symbols represent measured data, straight lines are linear regressions of measurements.
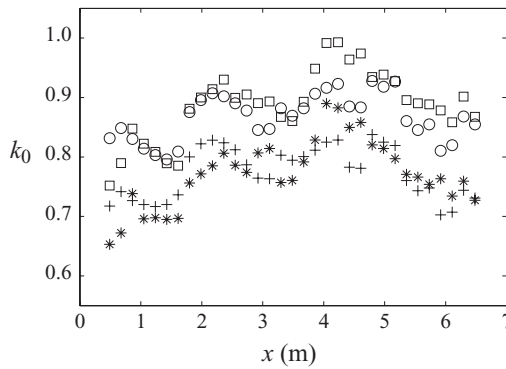

FIGURE 13. Scaling constant k_0 of the 4/3 law measured at different streamwise locations. $\bigcirc$, 1D diffusion assumption, $z^+ = 200$; $\square$, 1D diffusion assumption, $z^+ = 400$; +, 3D diffusion assumption, $z^+ = 200$; *, 3D diffusion assumption, $z^+ = 400$.

Combining all data measured from the two elevations at all streamwise locations, $k_0 = 0.87 \pm 0.13$ for the 1D diffusion case. The constant for the 3D diffusion case has a slightly lower value, $k_0 = 0.77 \pm 0.11$. The uncertainties presented here are ± 1.96 times the sample standard deviation of the measured k_0 at all locations (i.e. a 95% confidence interval). The same notation will be used for uncertainties of other measured parameters in this paper. For instance, $p = p_s \pm \delta p$, where p_s is the sample mean of the parameter p, and δp is 1.96 times the sample standard deviation. Therefore the relative error of k_0, denoted as $\delta k_0 / k_0$, is about 15% for the 1D case, and 14% for the 3D case.

The Richardson–Obukhov constant g has been the most important constant in the theory of relative dispersion. It is easier to estimate g than to estimate k_0 from experimental or numerical studies, as the former can be determined by tracking two particles, or following a dispersing cloud, while the latter requires examining the evolution of the p.d.f. of separation (or the distance-neighbour function). As discussed in the introduction, g is closely related to k_0. If both the 4/3 law (according to Richardson's postulation, i.e. $K_R \sim l^{4/3}$) and the t^3 growth of the mean-square
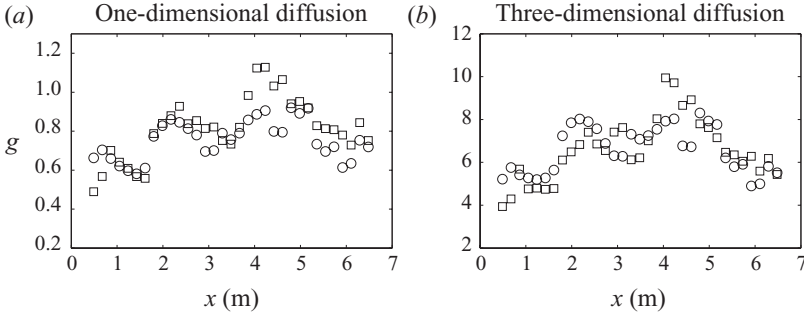
FIGURE 14. Measured Richardson–Obukhov constant g at different streamwise locations. $\circ$, $z^+ = 200$; $\square$, $z^+ = 400$.

separation are true, $g = (280/243)k_0^3$ for the 1D diffusion equation (1.8), and $g = (1144/81)k_0^3$ for the 3D diffusion equation (1.14).

Calculated g values at all streamwise locations are plotted in figure 14. With the assumption of a 1D diffusion process, and combining data from both elevations, $g = 0.77 \pm 0.29$, while with the 3D assumption, $g = 6.49 \pm 2.72$, which is much higher. Hence the relative error, $\delta g/g$, is 38 % for the 1D case and 42 % for the 3D case.

Despite these uncertainties, the measured $K_R(l)$ profiles in the near field agree well with those in the far field in shape (see figures 11 and 12), suggesting that the uncertainties of estimated values of both k_0 and g may be mostly due to the approximation of $\partial Q/\partial t$ using $U(\partial Q/\partial x)$. It is difficult to identify all the sources of random errors for the two constants. In particular the uncertainties associated with spatial gradients of Q and q_C and the numerical integral of them over l can not be easily determined. However, the propagation of uncertainties from the errors of U and ϵ can be evaluated. Ignoring other sources of errors, $k_0 \sim U\epsilon^{-1/3}$ and $g \sim U^3\epsilon^{-1}$. Thus the relative errors can be estimated as

$$\frac{\delta k_0}{k_0} = \frac{\delta U}{U} + \frac{1}{3}\frac{\delta\epsilon}{\epsilon} \quad \text{and} \quad \frac{\delta g}{g} = 3\frac{\delta U}{U} + \frac{\delta\epsilon}{\epsilon}. \tag{4.15}$$

In this study, the streamwise mean velocity U is taken as the local ensemble mean averaged over the spanwise (y) direction, since the plume meanders laterally. However, due to the existence of a cellular secondary flow structure (see the discussion on velocity spectra in §3), the spanwise variation of U in terms of 1.96 times the standard deviation is about 6–9 %. If the spanwise variation is the major source of uncertainty for local measurement of U, $\delta U/U \approx 7.5$ %. The dissipation rate ϵ is also a spanwise-averaged value, and $\delta\epsilon/\epsilon \approx 8$ %. According to (4.15), the contribution from the errors of U and ϵ is 10.2 % to $\delta k_0/k_0$ and is 30.5 % to $\delta g/g$. Therefore, nearly 2/3 of the random errors of the estimated k_0 and g are due to the uncertainties of U and ϵ.

The estimated $g = 0.77 \pm 0.29$, based on the assumption of a 1D diffusion equation, is of the same order as those estimated in other recent studies. For example, $g = 0.5 \pm 0.2$ according to laboratory 3D particle tracking experiments (Ott & Mann 2000); $g = 0.8 \sim 1.8$ for stochastic models (Borgas & Sawford 1994); $g = 0.7$ according to the DNS by Ishihara & Kaneda (2002); $g = 0.55 \pm 0.05$ for forward relative dispersion from both particle tracking experiments and DNS data (Berg *et al.* 2006); and more

recently Franzese & Cassiani (2007) provided an analytical derivation of g which depends on Re_λ, and g converges to 0.7 as Re_λ becomes large.

However, our estimation of g with the assumption of 3D diffusion is almost an order of magnitude higher. It should be noted that the true 3D format of distance-neighbour function q may not be locally isotropic in this case. The turbulent velocity field in the boundary layer is not isotropic either, although some 1D velocity spectra show a $-5/3$ power law. Similarly, the evidence of $l^{4/3}$ scaling for the measured K_R and K_C may not indicate a local isotropy of q. Therefore the conversion from the 1D distance-neighbour function Q to the 3D q following the assumption of a conditional p.d.f. could be wrong, or a biased estimation at least.

Estimated g from both the 1D and 3D models is probably overestimated. This is due to the substitution of $\partial/\partial t$ with $(1/U)(\partial/\partial x)$. The scalar concentration measured at $z^+ = 200$ and $z^+ = 400$ contains tracer dye coming from all other elevations at an earlier time as a result of vertical mixing. Therefore, a better estimate of mean velocity that can be used to estimate $\partial/\partial t$ is the speed of the crossflow COM of the plume, i.e.

$$U_m = \frac{\displaystyle\int\int C(y,z)U(y,z)\,\mathrm{d}z\,\mathrm{d}y}{\displaystyle\int\int C(y,z)\,\mathrm{d}z\,\mathrm{d}y}. \tag{4.16}$$

This velocity, however, is not available from the experiments. 2D PIV–LIF measurement on a vertical plane near the centreline of the mean plume was conducted only at $x = 3.67$ m. The depth-averaged velocity weighted by the vertical distribution of the mean scalar concentration is about 85 % of U measured at $z^+ = 200$. Using this reduced velocity, mean values of g would be changed from 0.77 to 0.47 for the 1D case, and from 6.49 to 3.99 for the 3D case. It should be noted that g is very sensitive to the change of U, as $g \sim U^3 \epsilon^{-1}$. Also, any underestimate of ϵ would result in an overestimate of g. In this study, the dissipation rate is estimated as ϵ_A using (3.4) following the assumption of local axisymmetry, which is the lowest among estimates using other methods (see figure 5). Hence k_0 and g could also be overestimated due to the possible underestimation of ϵ.

4.4. *An extended model for the relative diffusivity K_R*

In the following two subsections, we discuss the dispersion of the continuously released plume as a whole. Specifically, how dispersion at larger scales can be linked to the internal scaling, i.e. the 4/3 law in the inertial range. Although inner scaling dispersion is intrinsically 3D, the following discussion is based on the 1D diffusion model for practical reasons. First, the characteristic width of the plume σ is directly related to the 1D distance-neighbour function $Q(l, x)$. Second, measured 1D diffusivities K_R in the inertial range at all streamwise locations are consistent, although this is not a justification that the 1D diffusion model is true.

The 4/3 law is only valid if the separation length falls into the inertial subrange. As the separation length l approaches the integral length scale L and beyond, K_R approaches a constant value ($\sim \delta_v L$) asymptotically (see figure 11). Based on the PIV measurements of the turbulence structure, we found the following model for relative diffusivity agrees very well with the measured K_R at both small (inertial range scale) and large (integral scale) separation lengths. The proposed model, denoted as K_m, is
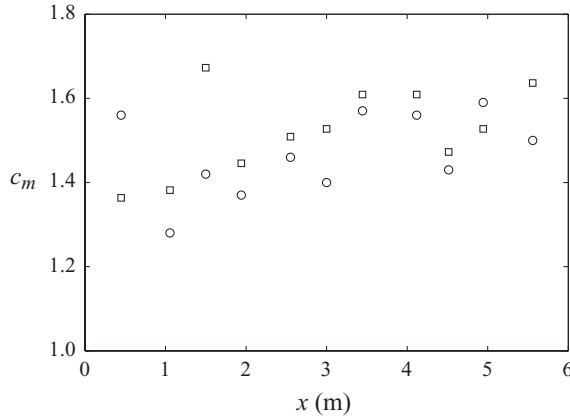
$$K_m = c_m u_m l_m, \tag{4.17}$$

FIGURE 15. Determined coefficients in the model of relative diffusivities.
$\bigcirc$, $z^+ = 200$; $\square$, $z^+ = 400$.

where c_m is a constant to be determined, and the model velocity scale u_m and model length scale l_m are both functions of the separation l. For a pair of particles at any instant, only the difference between their velocities is responsible for dispersion. Thus the velocity scale in the model is defined as the square root of the lateral structure function of the turbulence field, namely

$$u_m(l) = \sqrt{\overline{[v(y) - v(y + l)]^2}}. \tag{4.18}$$

According to Kolmogorov's law of universal similarity, u_m defined in such a way should scale with $(\epsilon l)^{1/3}$ in the inertial subrange. As l gets large enough ($\sim L$), $v(y)$ and $v(y + l)$ become uncorrelated and $u_m = \sqrt{2}\delta_v$.

The length scale l_m is modelled as

$$l_m(l) = \int_0^l \rho_{vy}(l') \, \mathrm{d}l', \tag{4.19}$$

where ρ_{vy} is the lateral auto-correlation coefficient of the velocity field, i.e.

$$\rho_{vy}(l) = \frac{\overline{v(y)v(y + l)}}{\delta_v^2}. \tag{4.20}$$

This definition suggests that as l becomes large, $l_m \sim L$. Thus at a large separation distance, $K_m \sim \delta_v L$.

The constant c_m is determined by fitting the measured K_R with the model K_m, and the results are shown in figure 15. Combining data from both elevations, $c_m = 1.40 \pm 0.21$.

The comparison between the model and measured relative diffusivities is shown in figure 16. The agreement is striking, considering the fact that K_R and K_m are obtained from the two independent measurements (PIV and LIF).

4.5. *'Apparent' diffusivity and relative diffusivity*

It should be noted that to our knowledge this is the first experimental determination of K_R. Previously relative dispersion was investigated by studying the growth rate of
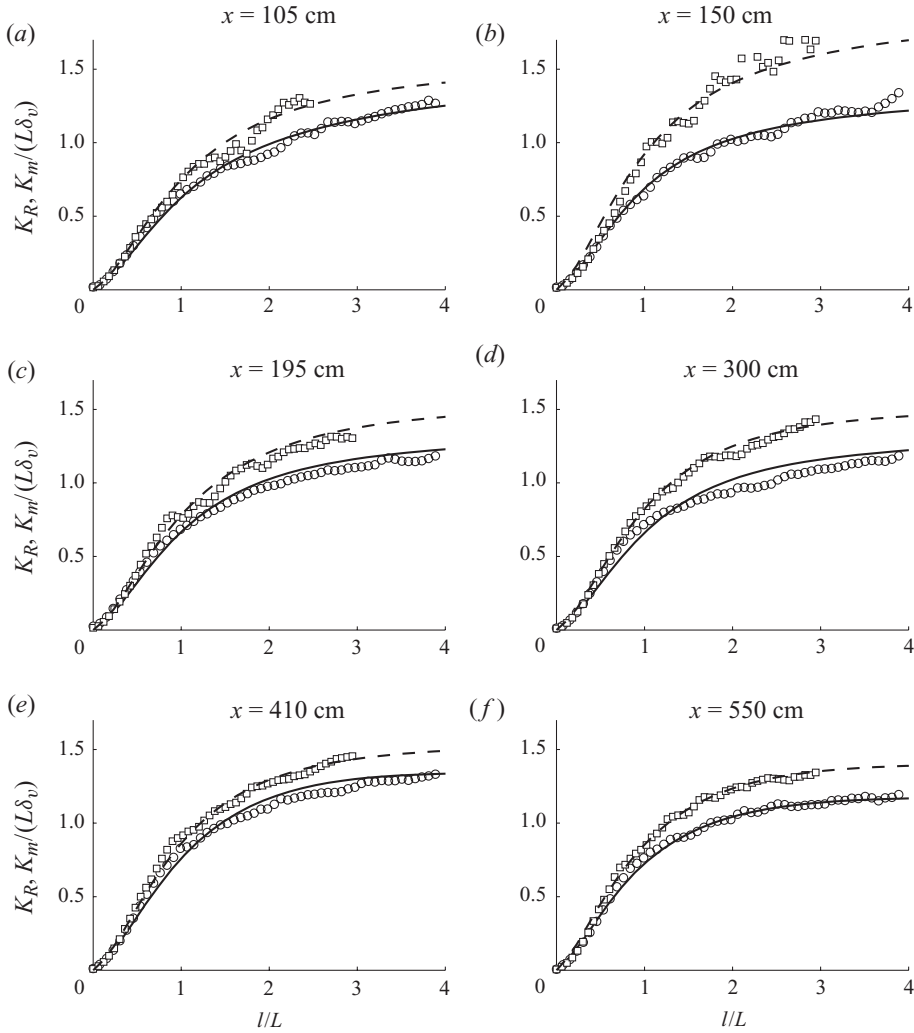
FIGURE 16. Comparison between the measured relative diffusivity K_R and the model relative diffusivity K_m. $\circ$, K_R on $z^+ = 200$; $\square$, K_R on $z^+ = 400$; —, K_m on $z^+ = 200$; $--$, K_m on $z^+ = 400$.

the mean-square size of a cloud or plume, which is different, and we denote this as the 'apparent' diffusivity K_A. K_A can be related to K_R by

$$K_A = \frac{1}{2}\frac{\partial \overline{\sigma^2}}{\partial t} = \frac{1}{4}\frac{\partial \overline{\int_{-\infty}^{\infty} l^2 q(l)\,\mathrm{d}l}}{\partial t} = \frac{1}{4}\frac{\partial \int_{-\infty}^{\infty} l^2 Q(l)\,\mathrm{d}l}{\partial t}$$

$$= \frac{1}{4}\int_{-\infty}^{\infty} l^2 \frac{\partial Q(l)}{\partial t}\,\mathrm{d}l = \frac{1}{4}\int_{-\infty}^{\infty} l^2 \frac{\partial}{\partial l}\left(K_R \frac{\partial Q}{\partial l}\right)\mathrm{d}l$$

$$= \frac{1}{2}\int_{-\infty}^{\infty}\left(K_R + l\frac{\partial K_R}{\partial l}\right)Q\,\mathrm{d}l. \tag{4.21}$$

Thus K_A depends not only on the properties of the turbulent velocity field, in terms of K_R, but also on the exact concentration distribution of a dispersing plume (or cloud), in terms of $Q(l)$. In most, if not all previous field experiments on relative dispersion, the size of the plume was much smaller than the eddy size which corresponds to the lower wavenumber limit of the inertial subrange, denoted as $\mathscr{L}$. We can assume $Q(\mathscr{L}) \approx 0$. Within the inertial subrange, it is commonly assumed that K_R is given by a power law $K_R \sim l^n$, where $n = 4/3$ in the case of 3D turbulence (Richardson's 4/3 law) and $n = 2$ in the case of large-scale 2D turbulence (Fong & Stacey 2003). From (4.21),

$$K_A \sim \int_{-\infty}^{\infty} l^n Q \, \mathrm{d}l. \tag{4.22}$$

Without specifying the exact shape of $Q(l)$, if we just assume that it is self-similar, such that

$$Q(l) = \frac{f\left(\dfrac{l}{\sigma}\right)}{\sigma}, \tag{4.23}$$

and substitute it into (4.22), we have

$$K_A \sim \int_{-\infty}^{\infty} \sigma^n \psi^n f(\psi) \, \mathrm{d}\psi = \sigma^n \int_{-\infty}^{\infty} \psi^n f(\psi) \, \mathrm{d}\psi \sim \sigma^n, \tag{4.24}$$

where $\psi \equiv l/\sigma$. Therefore, if the assumption of self-similarity were true and $\sigma < \mathscr{L}$, observed K_A would present the same power law as K_R does, thus the method based on plume size growth is valid. In the present study, however, the separation of large eddies (limited by the height above the channel bottom) from the viscous scales is small, and the plume quickly becomes larger than inertial scale eddies. As a result, the measured σ^2 does not show a t^3 tendency.

Up to this point, it has been clear that the turbulent relative diffusivity, which is responsible for the dispersion of the distance-neighbour function, is largely determined by the turbulent medium, regardless of the concentration field itself. On the other hand, according to (4.21), the apparent diffusivity is a weighted average of the relative diffusivity, i.e. average of $K_R + l(\mathrm{d}K_R/\mathrm{d}l)$, weighted by $Q(l)$, which is a property of the scalar distribution. This concept is illustrated in figure 17, which shows how the apparent diffusivity, as an overall property of turbulent diffusion, is derived.

The terms $K_R(l)$ and $l(\mathrm{d}K_R/\mathrm{d}l)$ are calculated from the measure turbulent velocity distribution, according to the proposed model equation (4.17). After normalization by δ_v and L, their distributions for all measurement locations are similar. The second term, $l(\mathrm{d}K_R/\mathrm{d}l)$, is relatively small, and peaks at around $l = L$. The distribution of $Q(K_R + l(\mathrm{d}K_R/\mathrm{d}l))$ is strongly affected by the shape of $Q(l)$. There is also a peak value in this distribution, and the corresponding separation length can be interpreted as the size of the eddy which is most responsible for the overall expansion of the plume. This eddy size has not increased much as the plume grows, but its relative contribution decreases significantly.

As a result the integration of $Q(K_R + l(\mathrm{d}K_R/\mathrm{d}l))$ over all l is carried out to calculate the apparent diffusivity. The results are compared with the measured K_A, and they agree very well, as shown in figure 18.
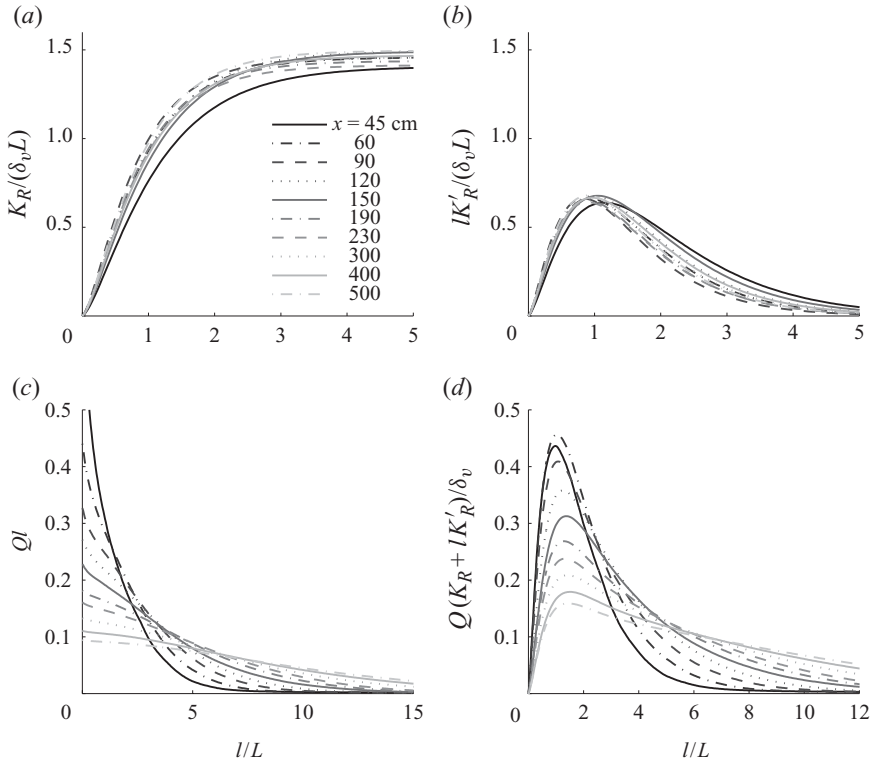
(*a*)

(*b*)

(*c*)

(*d*)

FIGURE 17. Contribution of relative diffusivity at different separation to the apparent diffusivity, measured at $z^+ = 200$.
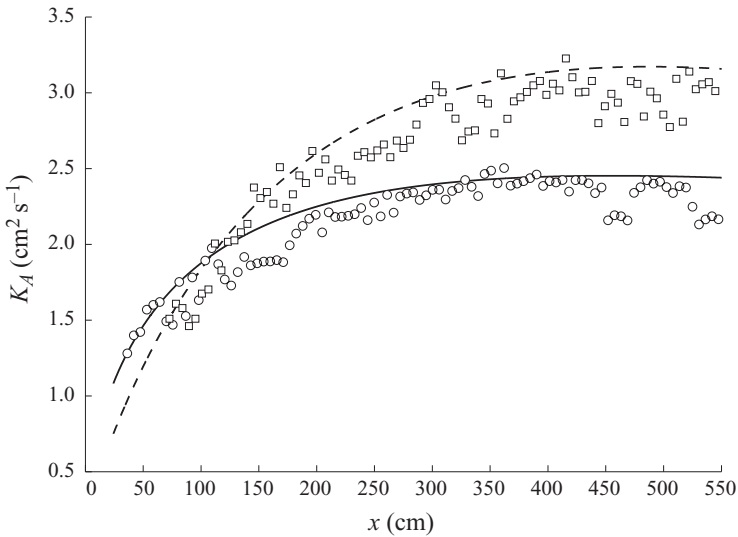
FIGURE 18. Verification of the relationship between relative diffusivity and apparent diffusivity, equation (4.21). —, measured K_A at $z^+ = 200$; ––, measured K_A at $z^+ = 400$; ○, K_A calculated from the model at $z^+ = 200$; □, K_A calculated from the model at $z^+ = 400$.

5. Conclusions

Recent advances in the theory of turbulent relative dispersion have focused on understanding and modelling the statistics of the spread of two fluid particles, as it is the fundamental physics that governs the diffusion of scalar concentrations as well as their fluctuations and spatial/temporal structures in turbulent media. In this paper, we present an alternative approach by measuring the turbulent concentration distribution of a passive scalar, the auto-correlation of which can be interpreted as the p.d.f. of separation distances of a cluster of particles in a turbulent flow. This approach is not new, having been proposed in concept by Richardson (1926), i.e. the distance-neighbour function, or the equivalent p.d.f. of particle pair separations; however, the accuracy and resolution of LIF measurements allow it to be examined in detail. The presented results are the first experimental evidence to support the hypothesis that simple diffusion equations (1.5) and (1.7) may be used to describe the evolution of the separation p.d.f. (Richardson 1926; Batchelor 1952; Monin & Yaglom 1975; Salazar & Collins 2009). Taking the cross-plume concentration correlation as the 1D format of the distance-neighbour function, the relative diffusivity (K_R) can be directly calculated from the measurements. The calculated K_R unambiguously show a 4/3 power-law scaling with the separation distance, l, in the inertial subrange. This result agrees with Richardson's hypothesis (Richardson 1926) and contradicts the statements made by Batchelor (1952), who argued that K_R should only depend on the local size of the spread of the scalar distribution and be independent of l. The difference between Batchelor's and Richardson's theories on K_R is significant as it results in very different scalar structures, i.e. a Gaussian versus non-Gaussian distribution of the separation p.d.f.. Since the 3D format of the distance-neighbour function cannot be determined experimentally in this study, it is estimated from the 1D format with the assumption of local isotropy. In this paper, the 1D distance neighbour function is interpreted as either a conditional p.d.f. or a marginal p.d.f. of the 3D function. While the marginal p.d.f. model does not show a 4/3 scaling, the conditional p.d.f. model does.

The estimated Richardson–Obukhov constant based on the 1D diffusion equation ($g = 0.77 \pm 0.29$) is close to those found in other recent studies. However, with the 3D diffusion equation and the conditional p.d.f. model, $g = 6.49 \pm 2.72$, which is almost an order of magnitude higher than that derived from the 1D diffusion equation. This large discrepancy may indicate: (i) the actual distance neighbour function resulting from a dispersing plume in a turbulent boundary layer may not be locally isotropic, just as the underlying turbulence itself is not locally isotropic; (ii) the relation between the measured 1D distance-neighbour function and the 3D distance-neighbour function may not be simply described as a conditional p.d.f. model; (iii) the Richardson–Obukhov constant g may take different values for 1D and 3D dispersion processes. The estimated scaling constant k_0 in the 4/3 scaling law is 0.87 ± 0.13 for the 1D diffusion equation and 0.77 ± 0.11 for the 3D diffusion equation. The difference between the 1D and 3D result is much smaller compared with that for g.

The uncertainties of g and k_0 are largely due to the estimation of $\partial/\partial t$ by $U(\partial/\partial x)$ and the uncertainties associated with the dissipation rate ϵ. Both g and k_0 are likely to be overestimated since the local mean velocity U is assumed to be the mean advection speed of a cloud or puff within the continuously released plume. This is almost certainly an overestimation as the plume is not vertically well mixed and the concentration decreases from the channel bottom to the water surface. Moreover, it should be noted that the experiment presented in this paper is a continuous plume

release from a flush-bed source into a turbulent boundary layer, not a 'pulse' release of puff. The obtained distance-neighbour function is not exactly the same as originally proposed by Richardson. Therefore, these results, including the two constants k_0 and g, may not be comparable to those obtained from tracking particle pairs in locally isotropic flows.

The Reynolds number of the flow in the present study is rather low ($R_\lambda \approx 150 \sim 170$), and the dependence of g on Reynolds number has not been addressed in this paper. This should be included in future studies.

Practically, for most turbulent scalar diffusion models, the property of the underlying turbulent flow is taken as the fundamental parameter that controls the spread and dilution of the concentration distribution, or the size of the distribution is included in some scale-dependent plume dispersion models (Stacey *et al.* 2000). According to (4.21), the actual concentration distribution should also be included, at least for determining the apparent diffusivity, the rate at which the squared size of the plume grows. On the other hand, the diffusion of the structure $Q(l, t)$ in separation space is only a function of the flow field. Experimental results suggest that within the inertial subrange scale, K_R is universally determined by the dissipation rate for equilibrium turbulence. Also, the extended 1D model for K_R proposed in this paper is completely based on the Eulerian structure of turbulence, and it agrees well with measured K_R at both inertial subrange and integral scales.

It should be noted that the effect of the actual concentration distribution on the turbulent scalar diffusivity may not be as important if the spread of concentration is much larger than the inertial scales of the turbulence. At integral scales, the relative diffusivity approaches a constant value which scales with the external scales of the turbulence, and the concentration distribution de-correlates at large scales. The integral in (4.21) will become a constant value, if the distance-neighbour function also develops to an equilibrium state. Therefore, relative dispersion and the effect of the concentration distribution are only significant for small size plumes, relative to the largest scales of the turbulence, or the structure of scalar fluctuations within the inertial scales. For example, greater understanding of the relative diffusion equation may help to answer some scientific questions related to the olfactory function of odour plume tracking animals, such as lobsters, crabs, dogs and moths. These animals have developed robust and efficient chemotactic algorithms to track odours to their sources in a turbulent surrounding environment (Murlis, Elkinton & Carde 1992; Atema 1995). Hydrodynamic studies on the 'sniffing' of a lobster have been conducted by Koehl *et al.* (2001) by stroking an antennule of a real lobster (*Panulirus argus*) with the same speed at which it 'sniffs' into a 'odour' plume containing fine scale structures, and the results indicated these structures can be captured and well preserved in the array of chemosensory hairs on the surface of the antennule. Lobsters may use the distribution of the fine concentration structure to search for targets (sources). According to the present study, the evolution of small-scale scalar structures is statistically determined by the diffusion equation of the distance-neighbour function, thus an inverse solution can help to discover information related to the source, such as its size, distance, and direction relative to the current position.

Appendix A. Relation between particle separation probability density function and the distance-neighbour function

For a dispersing 'cloud' or 'puff' in a homogeneous and isotropic turbulent flow with concentration distribution $c(\boldsymbol{x}, t)$, the distance-neighbour function is then essentially the spatial auto-correlation of concentration:

$$\overline{q(\boldsymbol{l}, t)} = \frac{\overline{\int_V c(\boldsymbol{x}, t c(\boldsymbol{x} + \boldsymbol{l}, t)\,\mathrm{d}\boldsymbol{x}}}{M^2(t)}, \tag{A 1}$$

where $M(t) = \overline{\int_V c(\boldsymbol{x}, t)\,\mathrm{d}\boldsymbol{x}}$ which is the total mass, and the overbar means ensemble averaging over many trials. Assume the cloud originates from a 'pulse' release source with distribution $S(\boldsymbol{y}, s) = S(\boldsymbol{y})\delta(s)$, and $\int_V S(\boldsymbol{y})\,\mathrm{d}\boldsymbol{y} = M$ according to conservation of mass. Therefore,

$$\overline{q(\boldsymbol{l}_0, s)} = \frac{\overline{\int_V S(\boldsymbol{y})S(\boldsymbol{y} + \boldsymbol{l}_0)\,\mathrm{d}\boldsymbol{y}}}{M^2}. \tag{A 2}$$

Following (1.3),

$$\overline{c(\boldsymbol{x}, t)c(\boldsymbol{x} + \boldsymbol{l}, t)} = \int_V \int_V p_2(\boldsymbol{x}, \boldsymbol{x} + \boldsymbol{l}, t \mid \boldsymbol{y}, \boldsymbol{y} + \boldsymbol{l}_0, s)S(\boldsymbol{y})S(\boldsymbol{y} + \boldsymbol{l}_0)\,\mathrm{d}\boldsymbol{y}\,\mathrm{d}\boldsymbol{l}_0. \tag{A 3}$$

Dividing (A 3) by M^2 and then integrating over $\boldsymbol{x}$, and using (1.4), we have

$$\begin{aligned}
\overline{q(\boldsymbol{l}, t)} &= \int_V \int_V p_2(\boldsymbol{x}, \boldsymbol{x} + \boldsymbol{l}, t \mid \boldsymbol{y}, \boldsymbol{y} + \boldsymbol{l}_0, s)\,\mathrm{d}\boldsymbol{x}\,\frac{\int_V S(\boldsymbol{y} + \boldsymbol{l}_0)\,\mathrm{d}\boldsymbol{y}}{M^2}\,\mathrm{d}\boldsymbol{l}_0 \\
&= \int_V p_\Delta(\boldsymbol{l}, t \mid \boldsymbol{l}_0, s)\overline{q(\boldsymbol{l}_0, s)}\,\mathrm{d}\boldsymbol{l}_0.
\end{aligned} \tag{A 4}$$

Hence (1.6) is proved.

Multiplying the diffusion equation of particle separation p.d.f. (1.5) by $\overline{q(\boldsymbol{l}_0, s)}$ and integrating over $\boldsymbol{l}_0$, we get

$$\int_V \frac{\partial p_\Delta}{\partial t}\overline{q(\boldsymbol{l}_0, s)}\,\mathrm{d}\boldsymbol{l}_0 = \int_V \nabla \cdot [K_R \nabla p_\Delta]\,\overline{q(\boldsymbol{l}_0, s)}\,\mathrm{d}\boldsymbol{l}_0, \tag{A 5}$$

where the operator ∇ means taking gradient over $\boldsymbol{l}$, thus

$$\frac{\partial}{\partial t}\int_V p_\Delta\overline{q(\boldsymbol{l}_0, s)}\,\mathrm{d}\boldsymbol{l}_0 = \nabla \cdot \left[K_R \nabla \int_V p_\Delta\overline{q(\boldsymbol{l}_0, s)}\,\mathrm{d}\boldsymbol{l}_0\right]. \tag{A 6}$$

According to (1.6) which was just proved, (A 6) becomes

$$\frac{\partial \overline{q}}{\partial t} = \nabla \cdot [K_R(l)\nabla \overline{q}], \tag{A 7}$$

which is equation (1.7).

Through the above analysis, the dynamics of particle pair dispersion can be associated with the relative dispersion of a 'cloud' or 'puff'. If a diffusion equation can be applied to describe the p.d.f. of the particle pair separation, it can also be applied to the distance-neighbour function. Both equations share the same diffusion coefficient $K_R(l, t)$.

Appendix B. Relationship between the one-dimensional and three-dimensional isotropic distance-neighbour function

Denote the general 3D form of the distance neighbour function as $f(\boldsymbol{l}, t) = f(l_1, l_2, l_3, t)$. Assuming an isotropic distribution, f is radially symmetric, i.e. $f = q(l, t)$, where $l = \sqrt{l_1^2 + l_2^2 + l_3^2}$. Thus the diffusion equation is mathematically 1D, i.e. equation (1.14). In this paper, the cross-plume concentration correlation obtained experimentally, $Q(l, t)$, can be interpreted as a 1D representation of $q(l, t)$. There are two ways that they could be associated with each other.

(i) $Q(l_x, t)$ can be considered as a marginal p.d.f. of $f(l_1, l_2, l_3, t)$, i.e. Q is the integral of q in one direction (l_1) over the other two directions (l_2, l_3):

$$Q(l_1, t) = \int_{-\infty}^{\infty} \int_{-\infty}^{\infty} f(l_1, l_2, l_3, t) \, dl_2 \, dl_3. \tag{B 1}$$

The integration is over the plane of fixed l_1. Due to the radial symmetry of q, it can be written as

$$Q(l_1, t) = \int_{0}^{\infty} q(l, t) 2\pi h \, dh, \tag{B 2}$$

where $h = \sqrt{l^2 - l_1^2}$, or $\sqrt{l_2^2 + l_3^2}$, and $2\pi h \, dh = 2\pi l \, dl$. Therefore,

$$Q(l_1, t) = \int_{l_1}^{\infty} q(l, t) 2\pi l \, dl. \tag{B 3}$$

Taking the derivative with respect to l_1,

$$\frac{\partial Q(l_1, t)}{\partial l_1} = -q(l_1, t) 2\pi l_1. \tag{B 4}$$

Replacing l_1 by l, the 3D form of the distance-neighbour function, here denoted as q_M, can be related to Q as

$$q_M(l, t) = -\frac{1}{2\pi l} \frac{\partial Q(l, t)}{\partial l}. \tag{B 5}$$

(ii) $Q(l_1, t)$ can also be considered as the conditional p.d.f. of $f(l_1, l_2, l_3, t)$, i.e.

$$Q(l_1, t) = f_C(l_1, t | l_2 = 0, l_3 = 0) = \frac{f(l_1, l_2 = 0, l_3 = 0, t)}{f_M(l_2 = 0, l_3 = 0, t)}, \tag{B 6}$$

where $f_M(l_2 = 0, l_3 = 0, t)$ is the marginal p.d.f. of $f(l_1, l_2, l_3, t)$, while $l_2 = 0$ and $l_3 = 0$:

$$f_M(l_2 = 0, l_3 = 0, t) = \int_{-\infty}^{\infty} f(l_1, l_2 = 0, l_3 = 0, t) \, dl_1 = 2 \int_{0}^{\infty} q(l_1, t) \, dl_1. \tag{B 7}$$

From (B 6) and (B 7), it is clear that

$$f(l_1 = l, l_2 = 0, l_3 = 0, t) = q(l, t) = 2Q(l, t) \int_{0}^{\infty} q(l, t) \, dl. \tag{B 8}$$

Thus, $Q(l, t)$ has the same shape as $q(l, t)$ but they are normalized in different ways: $\int_{0}^{\infty} Q(l) \, dl = 1$, while $\int_{0}^{\infty} 4\pi l^2 q(l, t) \, dl = 1$. Multiplying (B 8) by $4\pi l^2$ and integrating over l,

$$1 = 8\pi \int_{0}^{\infty} l^2 Q(l, t) \, dl \int_{0}^{\infty} q(l, t) \, dl. \tag{B 9}$$

It should be noted that $\int_0^\infty l^2 Q(l,t)\,dl = 2\sigma^2(t)$ (see (4.7) and (4.8)), therefore $\int_0^\infty q(l,t)\,dl = 1/16\pi\sigma^2$. Substituting it into (B 8), the relationship between $Q(l,t)$ and $q(l,t)$ (here it is denoted as $q_C(l,t)$) can be established:

$$q_C(l,t) = \frac{Q(l,t)}{8\pi\sigma^2}. \tag{B 10}$$

REFERENCES

ATEMA, J. 1995 Chemical signals in the marine environment: dispersal, detection and temporal signal analysis. *Proc. Natl Acad. Sci* **92**, 62–66.

BATCHELOR, G. K. 1952 Diffusion in a field of homogeneous turbulence. II. The relative motion of particles. *Proc. Camb. Phil. Soc.* **48**, 345–362.

BERG, J., LÜTHI, B., MANN, J. & OTT, S. 2006 Backwards and forwards relative dispersion in turbulent flow: an experimental investigation. *Phys. Rev.* E **74** (1), 016304.

BIFERALE, L., BOFFETTA, G., CELANI, A., DEVENISH, B. J., LANOTTE, A. & TOSCHI, F. 2005 Lagrangian statistics of particle pairs in homogeneous isotropic turbulence. *Phys. Fluids* **17** (11), 115101.

BORGAS, M. S. & SAWFORD, B. L. 1994 A family of stochastic models for two-particle dispersion in isotropic homogeneous stationary turbulence. *J. Fluid Mech.* **279**, 69–99.

BOURGOIN, M., OUELLETTE, N. T., XU, H., BERG, J. & BODENSCHATZ, E. 2006 The role of pair dispersion in turbulent flow. *Science* **311**, 835–838.

COWEN, E. A., CHANG, K. A. & LIAO, Q. 2001 A single-camera coupled PTV-LIF technique. *Exp. Fluids* **31**, 63–73.

COWEN, E. A. & MONISMITH, S. G. 1997 A hybrid digital particle tracking velocimetry technique. *Exp. Fluids* **22**, 199–211.

CSANADY, G. T. 1963 Turbulent diffusion in lake huron. *J. Fluid Mech.* **17**, 360–384.

DORON, P., BERTUCCIOLI, L., KATZ, J. & OSBORN, T. R. 2001 Turbulence characteristics and dissipation estimates in the coastal ocean bottom boundary layer from PIV data. *J. Phys. Oceanogr.* **31** (8), 2108–2134.

DURBIN, P. A. 1980 A stochastic model of two-particle dispersion and concentration fluctuations in homogeneous turbulence. *J. Fluid Mech.* **100**, 279–302.

FONG, D. & STACEY, M. 2003 Horizontal dispersion of a near-bed coastal plume. *J. Fluid Mech.* **489**, 239–267.

FRANZESE, P. & CASSIANI, M. 2007 A statistical theory of turbulent relative dispersion. *J. Fluid Mech.* **571**, 391–417.

GEORGE, W. K. & HUSSEIN, H. J. 1991 Locally axisymmetric turbulence. *J. Fluid Mech.* **233**, 1–23.

GIFFORD, F. J. 1957 Relative atmospheric diffusion of smoke puffs. *J. Meteorol.* **14**, 410–414.

ISHIHARA, T. & KANEDA, Y. 2002 Relative diffusion of a pair of fluid particles in the inertial subrange of turbulence. *Phys. Fluids* **14** (11), L69–L72.

KARCZ, I. 1966 Secondary currents and the configuration of a natural stream bed. *J. Geophys. Res.* **71**, 3109–3116.

KOEHL, M. A. R., KOSEFF, J. R., CRIMALDI, J. P., MCCAY, M. G., COOPER, T., WILEY, M. B. & MOORE, P. A. 2001 Lobster sniffing: antennule design and hydrodynamic filtering of information in an odor plume. *Science* **294**, 1948–1951.

KOLMOGOROV, A. N. 1941 Dissipation of energy in locally isotropic turbulence. *Dokl. Akad. Nauk SSSR* **32**, 19–21.

LIAO, Q. & COWEN, E. A. 2005 An efficient anti-aliasing spectral continuous window shifting technique for PIV. *Exp. Fluids* **38** (2), 197–208.

MONIN, A. S. & YAGLOM, A. M. 1975 *Statistical Fluid Mechanics*, Vol. 2. MIT Press.

MURLIS, J., ELKINTON, J. S. & CARDE, R. T. 1992 Odor plumes and how insects use them. *Annu. Rev. Entomol.* **37**, 505–532.

OBUKHOV, A. M. 1941 Spectral energy distribution in turbulent flow. *Izv. Akad. Nauk SSSR Ser. Geogr. Geofiz.* **5**, 452–566.

OKUBO, A. 1971 Oceanic diffusion diagrams. *Deep-Sea Res.* **18**, 789–802.

OTT, S. & MANN, J. 2000 An experimental investigation of the relative diffusion of particle pairs in three-dimensional turbulent flow. *J. Fluid Mech.* **422**, 207–223.

OUELLETTE, N. T., XU, H., BOURGOIN, M. & BODENSCHATZ, E. 2006 An experimental study of turbulent relative dispersion models. *New J. Phys.* **8**, Art. No. 109.

POPE, S. B. 2000 *Turbulent Flows*. Cambridge University Press.

RICHARDSON, L. F. 1926 Atmospheric diffusion shown on a distance-neighbour graph. *Proc. R. Soc. Lond.* A (110), 709–727.

SADDOUGHI, S. G. & VEERAVALLI, S. V. 1994 Local isotropy in turbulent boundary layers at high Reynolds number. *J. Fluid Mech.* **268**, 333–372.

SALAZAR, J. P. L. C. & COLLINS, L. R. 2009 Two-particle dispersion in isotropic turbulent flows. *Annu. Rev. Fluid Mech.* **41**, 405–432.

SAWFORD, B. 2001 Turbulent relative dispersion. *Annu. Rev. Fluid Mech* **33**, 289–317.

SPALART, P. R. 1988 Direct simulation of a turbulent boundary-layer up to $R_\theta = 1410$. *J. Fluid Mech.* **187**, 61–98.

STACEY, M. T., COWEN, E. A., POWELL, T. M., DOBBINS, E., MONISMITH, S. G. & KOSEFF, J. R. 2000 Plume dispersion in a stratified near-coastal flow: measurements and modeling. *Cont. Shelf Res.* **20** (6), 637–663.

STOMMEL, H. 1949 Horizontal diffusion due to oceanic turbulence. *J. Mar. Res.* **8**, 199–225.

SULLIVAN, P. J. 1971 Some data on the distance-neighbour function for relative diffusion. *J. Fluid Mech.* **47**, 601–607.

THOMSON, D. J. 1990 A stochastic model for the motion of particle pairs in isotropic high-Reynolds-number turbulence, and its applications to the problem of concentration variance. *J. Fluid Mech.* **210**, 113–153.

VANOI, V. A. 1946 Transportation of suspended sediment by water. *Trans. ASCE* **111**, 67–133.

YEUNG, P. K. & BORGAS, M. S. 2004 Relative dispersion in isotropic turbulence. Part 1. Direct numerical simulations and Reynolds-number dependence. *J. Fluid Mech.* **503**, 933–124.

ZARRUK, G. A. & COWEN, E. A. 2008 Simultaneous velocity and passive scalar concentration measurements in low Reynolds number neutrally buoyant turbulent round jets. *Exp. Fluids* **44** (6), 865–872.